

Section 2: Heat Transfer and Fluid Mechanics

A Study on the Accuracy of Low and Higher Order BEM in Three-Dimensional Potential Flows Past Ellipsoids

J.Baltazar¹, J.A.C.Falcão de Campos² and J.Bosschers³

¹ Instituto Superior Técnico (IST), Department of Mechanical Engineering, Av. Rovisco Pais 1, 1049-001, Portugal, baltazar@marine.ist.utl.pt

² Instituto Superior Técnico (IST), Department of Mechanical Engineering, Av. Rovisco Pais 1, 1049-001, Portugal, fcampos@hidro1.ist.utl.pt

³ Maritime Research Institute Netherlands (MARIN), PO Box 28, 6700 Wageningen, the Netherlands, j.bosschers@marin.nl

Keywords: 3D Potential Flow, Higher Order Panel Method, Ellipsoid.

Abstract. In this paper we examine the errors due to different surface discretizations in the BEM solution of the potential flow past an ellipsoid. Three different approaches are considered: a low order method (LO), a second order normal calculation combined with the low order formulation (HO-normal) and a higher order panel geometry approximation (HO-geom). The potential, velocity and pressure distribution obtained with the different approaches are compared with the analytical solution for a wing-like ellipsoid in the tip region using conventional and orthogonal surface grids. With the LO method, it is shown that the use of orthogonal grids introduces larger errors in the solution near the tip than the use of conventional grids. These errors are significantly reduced already by using a higher order approximation to the element geometry, which improves the surface metrics evaluation.

Introduction

The low order BEM for the potential flow calculation based on the Morino formulation [1] has been extensively used in the analysis of lifting surfaces and marine propellers. The method employs constant source and dipole distributions on hyperboloidal panels and it is known that this method is subject to significant errors in the tip region of lifting surfaces due to grid inadequacy and poor wake modeling [2]. Therefore, it is important to analyze and quantify the numerical discretization error in the BEM potential flow calculation.

In this paper we examine the errors of the solution for an ellipsoid with three unequal axes using different conventional and orthogonal grids. The ellipsoid is identical to a wing with a 2:1 elliptical plan-form and a 10% thick elliptical section and special attention is given to the solution behavior near the tip. Two types of numerical formulations were considered: i) a low order panel method (LO) with constant source and dipole distributions on hyperboloidal panels; ii) a second order geometry description by bi-quadratic elements. The latter was implemented in the panel method with constant dipole and source distributions to investigate whether the solution in the tip region could be improved. The inclusion of this refinement has been done in two ways: either, only to improve the calculation of the normal to the surface, retaining the low order formulation for the panel method (HO-normal), or to fully allow for the second order panel geometry in the calculation of the influence coefficients and in the numerical surface differentiation (HO-geom).

BEM Formulation

Mathematical Model. The model adopted to describe the flow field around a hydrodynamic configuration is a potential flow model for inviscid and incompressible flow. Consider a three dimensional body with boundary S_B advancing with constant speed U_∞ in a domain extending to infinity in all directions.

The flow is steady and is assumed to be irrotational so that we may introduce a potential function Φ related to the flow velocity by $\vec{V} = \nabla\Phi$. We write for the potential $\Phi = \phi_\infty + \phi$, where ϕ_∞ is the potential of the undisturbed flow, $\vec{U}_\infty = \nabla\phi_\infty$, and ϕ is the perturbation potential due to the presence of the body. The perturbation potential satisfies the Laplace equation $\nabla^2\phi = 0$. The kinematic boundary condition $(\partial\phi/\partial n) = -\vec{U}_\infty \cdot \vec{n}$ is satisfied on the body surface S_B , where $\partial/\partial n$ denotes differentiation along the normal and \vec{n} is the unit vector normal to the surface directed outward from the body. At infinity the flow disturbance due to the body vanishes $\nabla\phi \rightarrow 0$.

By application of Green's second identity, assuming for the interior region to S_B , $\bar{\phi} = 0$, the integral representation of the potential at a point p on the body surface S_B is,

$$2\pi\phi(p) = \int_{S_B} \left[\phi(q) \frac{\partial}{\partial n_q} \left(\frac{1}{R(p,q)} \right) - \frac{\partial\phi}{\partial n_q} \frac{1}{R(p,q)} \right] dS, \quad (1)$$

where $R(p,q)$ is the distance between the field point p and the point q on the boundary S_B . With the $\partial\phi/\partial n_q$ on S_B known from the Neumann boundary condition on the body surface,

$$\frac{\partial\phi}{\partial n} \equiv \vec{n} \cdot \nabla\phi = -\vec{n} \cdot \vec{U}_\infty \text{ on } S_B. \quad (2)$$

Eq (2) is a Fredholm integral equation of the second kind on the unknown body surface potential $\phi(p)$.

Numerical Implementation. For the numerical solution of integral equation eq (1) we discretize the body surface S_B into a number of panels of known geometry, where the singularity distributions are assumed to vary in a prescribed way. The integral equation eq (1) is solved by the collocation method. The evaluation of the influence coefficients depends on the assumed geometry and singularity distributions for the panel. Three different approaches are considered: low order method (LO), a second order normal calculation combined with the low order formulation (HO-normal) and second order panel geometry method (HO-geom). A LU solver is used for the linear system of equations.

Low Order Method. In the standard low order approach the panel geometry is discretized by bi-linear quadrilateral elements which are defined by four points on the body surface. The collocation point is chosen as the element center point. We assume a constant strength of the dipole and source distributions on each panel. The influence coefficients are determined analytically using the formulations of Morino and Kuo [1]. The expressions are exact for the dipole influence coefficient. For the source influence coefficient the expressions are only exact for a plane panel.

Higher Order Normal Method. Alternatively, a second order geometry can be obtained using bi-quadratic panels defined by nine nodes on the body surface. Using this geometrical description, the surface metrics are calculated at the central point. This method combines the previous low-order formulation with a second order normal (calculated by the bi-quadratic panel description) in eq (2) and in the calculation of the tangential component of the undisturbed velocity.

Higher Order Geometry Method. In the higher order approach the panel geometry is discretized by bi-quadratic elements. The collocation point is chosen as the central point of the nine node element. In this case, the influence coefficients can not be evaluated analytically without further assumptions. Usually, if the integrations are carried out in the physical space, a small curvature expansion for the panel geometry and Taylor expansions for the singularities about the collocation point are assumed, [3]. If the integrations are carried out in the computational space, both the panel geometry and the singularities are expanded in

surface coordinates about the collocation points, [4]. Since, our purpose is to assess possible improvements resulting from the use of a second order formulation, the implementation of these approaches is not justified. In this way, we adopted a simpler numerical calculation of the influence coefficients, evaluated in a local panel coordinate system (ξ, η) . An adaptive integration algorithm, which provides a subdivision of the reference element, is used to achieve a specified numerical tolerance (10^{-6}) .

Calculation of Velocities and Pressure. From the potential solution on the surface the covariant surface velocity components are calculated by means of a second order differentiation scheme of the potential relative to the arc lengths on the body surface grid using periodic boundary conditions at the trailing edge. From Bernoulli's equation, the pressure coefficient C_p can be determined from $C_p = (p - p_\infty)/(1/2 \rho U_\infty^2) = 1 - \left(\vec{V} / U_\infty \right)^2$.

Results

Results are presented for an ellipsoid $\left(\frac{x}{a}\right)^2 + \left(\frac{y}{b}\right)^2 + \left(\frac{z}{c}\right)^2 = 1$ with $a = 1, b = 2, c = 0.1$ in a uniform onset flow aligned with the x axis. Two types of grids are investigated: i) conventional, with one family of lines defined by $y = const.$ and ii) orthogonal, generated by an algebraic procedure constructed by Eça [5]. Full cosine stretching is used in spanwise (y) and chordwise (x) directions. For the orthogonal grids the stretching is applied on the surface coordinate lines. For each type, 4 different grids have been generated with the number of panels $16 \times 8, 32 \times 16, 64 \times 32$ and 128×64 for the complete ellipsoid, where the first figure denotes the number of elements around each ellipsoid section along the chordwise direction and the second the number of sections. The grids generated by the algebraic procedure are not strictly orthogonal but were constructed to be practically orthogonal, having small deviations from orthogonality. For the finest grid, the maximum deviation is 12.6 degrees. At grid singularities, triangular elements are used with one node coincident with the singular point.

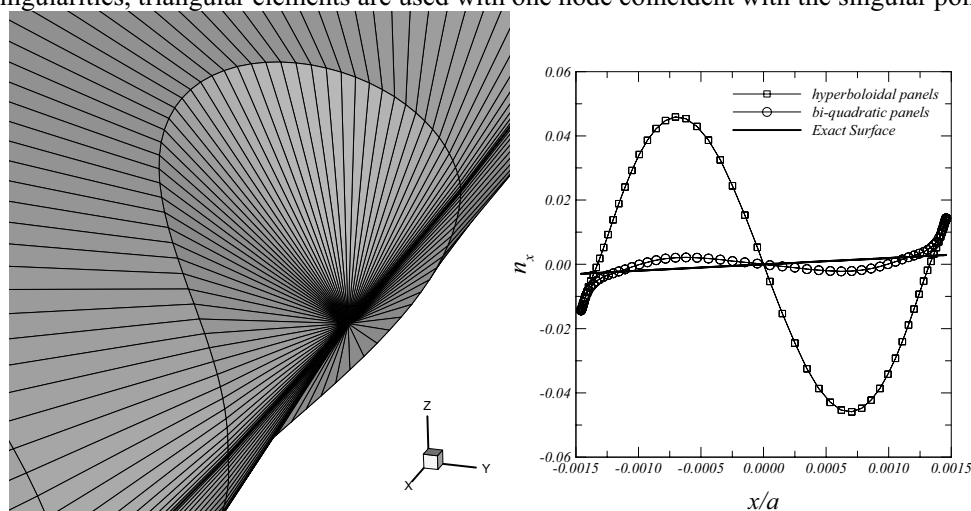


Figure 1 – (left): Perspective view of the tip region for the orthogonal grid. (right): Component along x of the normal in the last panel strip close to the tip.

Fig. 1(left) shows a perspective view of the tip region of the ellipsoid in the case of the 128×64 orthogonal grid. The poor approximation of the surface which is provided by the last strip of triangular panels is clearly seen. This poor approximation is reflected in the behavior of the normal to the surface obtained by the LO geometry formulation with hyperboloidal panels, as shown in Fig. 1(right). The normal shows a pronounced oscillation in the mid-chord region, which is absent in the exact surface. A considerable improvement in the calculation of the normal is obtained when a second order geometry description is introduced

with bi-quadratic panels. This large error in the normal at the tip is not present when using the conventional grid.

The comparison of the pressure coefficient calculated with the three different formulations and the analytical solution, [6], on the finest conventional and orthogonal grid are shown in Fig. 2 at the last panel strip close to the tip. For the conventional grid, it is seen that the use of a second order normal (HO-normal) in the low order solution or of a complete second order geometry formulation (HO) does not improve the solution. In the case of the orthogonal grid, there are considerable improvements due to the adoption of a higher order formulation for the geometry. The large error at mid-chord is considerably reduced. It is interesting to see that the low order formulation with the second order normal (HO-normal) already corrects most of the error in the low order solution. Note that in the case of the orthogonal grid the last panel strip is closer to the tip than in the case of the conventional grid, as seen in the values of the x/a coordinate.

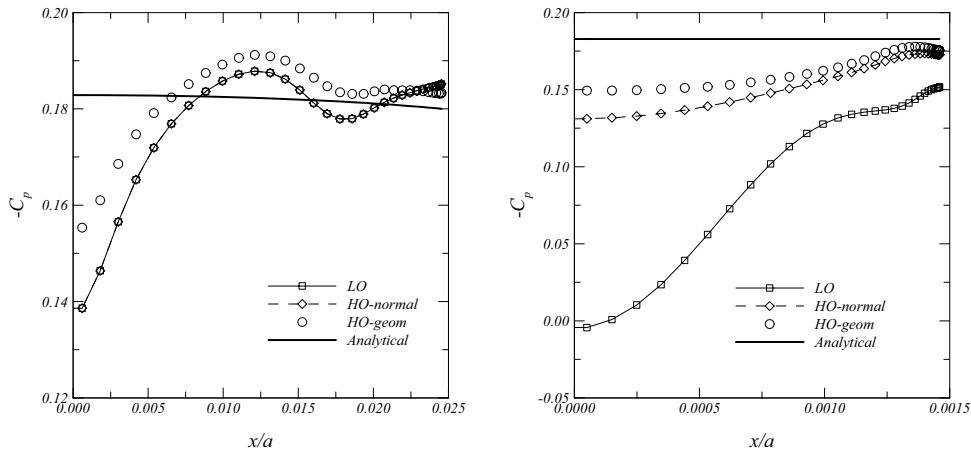


Figure 2 – Pressure distribution at last panel strip for the 128×64 conventional (left) and orthogonal grid (right). Comparison between the three different formulations and the analytical solution.

For the three formulations the L_∞ and L_2 error norms of the perturbation potential (made dimensionless by $U_\infty a$), pressure coefficient and perturbation surface velocity components are plotted as a function of the square-root of the number of panels in Fig. 3 for the conventional grids and in Fig 4 for the orthogonal grids. For the conventional grids, the HO-geom formulation leads to smaller errors than the LO and the HO-normal formulations. As expected, the differences between the LO and the HO-normal formulations are local at the tip and have less influence in the L_2 error norm. The maximum error norm of the perturbation surface velocity along the s_2 direction does not converge with grid refinement, probably because it is still not in the asymptotic convergence region due to the relative large panel width in s_2 direction. The absolute values are however much smaller than the perturbation velocities along the s_1 direction, so from a practical point of view the adopted grid refinement procedure is fully acceptable. For the orthogonal grids, the HO-normal already reduces the error norms for the perturbation potential and pressure coefficient, which proves the importance of a good geometrical approximation of the tip region. The error norms of the perturbation surface velocity along the s_2 direction do not converge. Due to the relative large panel spacing in the tip region (where the geometry changes significantly), the error levels of the pressure for the orthogonal grid are larger than those for the conventional grid. The application of a higher order geometry formulation leads to comparable results for the two grid types.

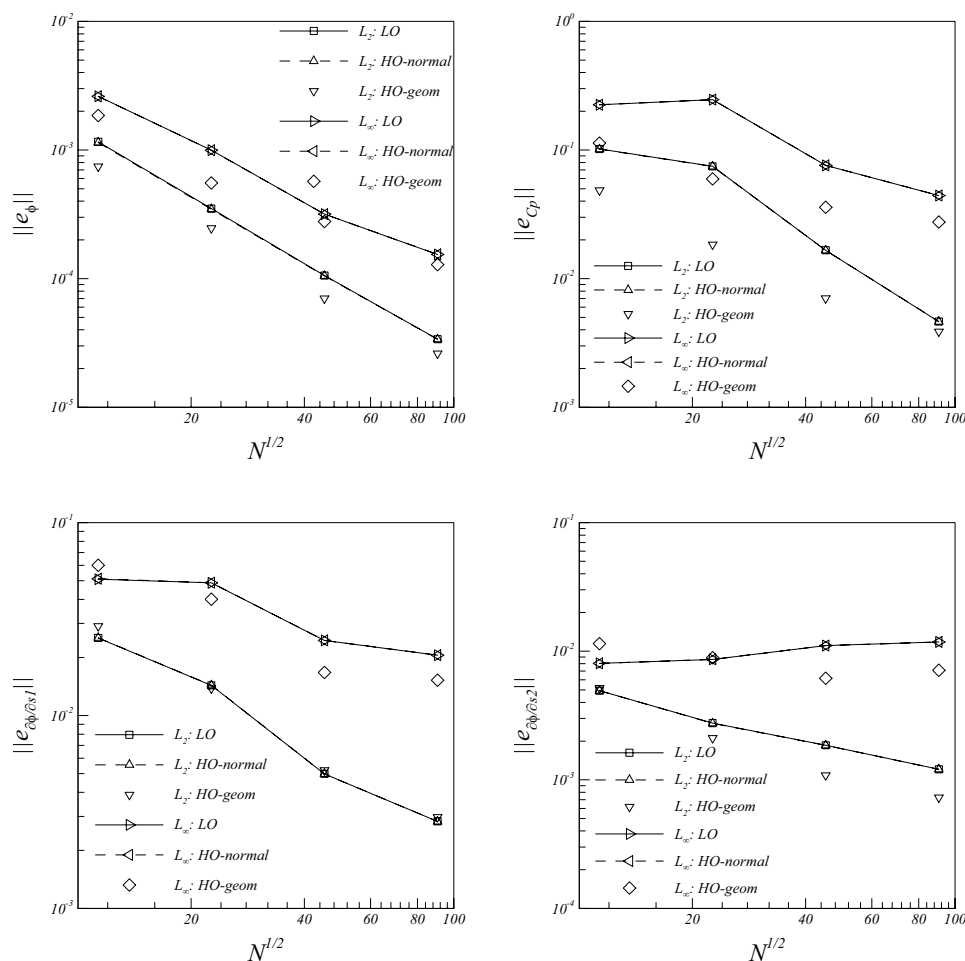


Figure 3 – Error norms of the perturbation potential (top-left), pressure coefficient (top-right), perturbation surface velocity $\partial\phi/\partial s_1$ (down-left) and $\partial\phi/\partial s_2$ (down-right) for the conventional grid.

Conclusions

In this paper an error norm analysis of a potential based Boundary Element Method is presented for two different grid types: conventional (grid lines along constant spanwise coordinate) and orthogonal. The application of a low order geometry approximation leads to large errors in the tip region for the orthogonal grid as compared to the conventional grid due to a larger discretization error and a large error in the normal in the tip panels. Therefore, two different higher order geometry approximations were implemented. One of the approximations involves only the normal of each panel. This leads to a large improvement in results for the orthogonal grid without additional computational burden. The further refinement of considering the complete second order geometry in the calculation of the influence coefficients (HO-geom) introduced an additional but less significant improvement in the potential flow solution. For the conventional grid only small improvements were obtained with the HO-geom formulation. With the higher order formulation the results for the conventional and orthogonal grid are of comparable accuracy.

Acknowledgments

The first author acknowledges the financial support granted by Fundação para a Ciência e a Tecnologia, Ph.D. grant SFRH/BD/14334/2003.

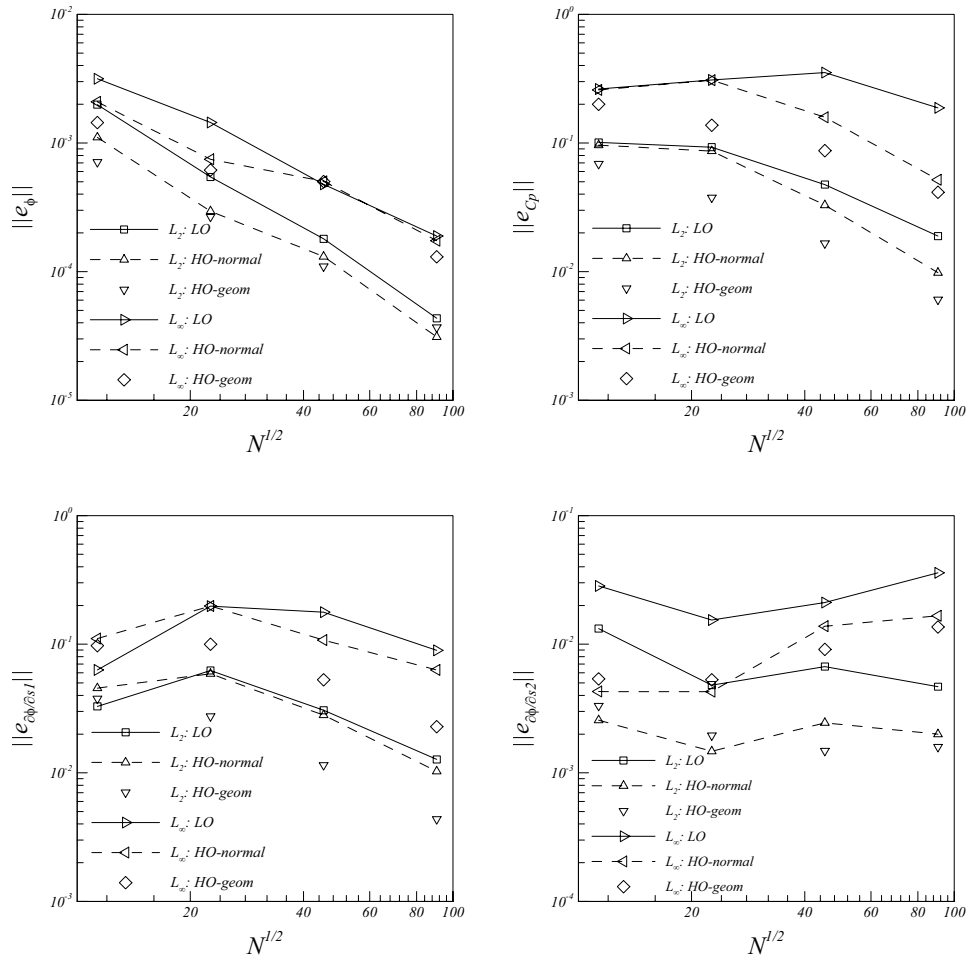


Figure 4 – Error norms of the perturbation potential (top-left), pressure coefficient (top-right), perturbation surface velocity $\partial\phi/\partial s_1$ (down-left) and $\partial\phi/\partial s_2$ (down-right) for the orthogonal grid.

References

- [1] L.Morino and C.C.Kuo *Subsonic Potential Aerodynamics for Complex Configurations: A General Theory*, AIAA Journal, Vol. 12, No. 2, 191-197 (1974).
- [2] S.Pyo and S.Kinnas *Propeller Wake Sheet Roll-up Modeling in Three Dimensions*, Journal of Ship Research, Vol. 41, No. 2, 81-92 (1997).
- [3] J.E.Romate *Local Error Analysis in 3-D Panel Methods*, Journal of Engineering Mathematics, 22, 123-142 (1988).
- [4] H.de Koning Gans *Numerical Time Dependent Sheet Cavitation Simulations using a Higher Order Panel Method*, Ph.D. Thesis, Delft University of Technology, (1994).
- [5] L.Eça, M.Hoekstra and J.Windt *Practical Grid Generation Tools with Applications to Ship Hydrodynamics*, 8th International Conference in Grid Generation in Computational Field Simulations, Hawaii, (2002).
- [6] H.Lamb *Hydrodynamics*, Sixth Edition, Cambridge University Press, (1975).

Transient Conduction and Convection Phenomena Across a Solid Layer Structure with Thermal Heterogeneities

A. Tadeu¹, N. Simões

¹ University of Coimbra, Department of Civil Engineering, Polo II- Pinhal de Marrocos, 3030-290 Coimbra, Portugal, tadeu@dec.uc.pt

Keywords: transient heat transfer, conduction, convection, Boundary Element Method, 2.5 Green's functions

Abstract. This paper describes the Green's functions for the steady-state response of a homogeneous three-dimensional solid layer formation bounded by two semi-infinite media, when subjected to a convective heat source placed somewhere in the media. These fundamental solutions are incorporated in a Boundary Element Method (BEM) formulation to compute the transient heat transfer by conduction and convection across a solid layer, which is buried in an unbounded medium, containing inclusions. The integration of the Green's functions in the BEM model avoids the full discretization of the layer interface boundaries. The technique first computes the solution in the frequency domain for a wide range of frequencies. Time series are then obtained by means of inverse Fourier transforms into space-time.

The proposed BEM code has been used to evaluate the heat field along a solid layer that contains heterogeneities. In order to understand the importance of the presence of multiple circular inclusions, different simulations analyses are modeled.

Introduction

The transient heat transfer is a fundamental field in several areas, such as thermal engineering problems. In building physics, the presence of thermal heterogeneities in construction elements affects their thermal behaviour, which can determine a poor performance relative to a dwelling's interior comfort.

The heat diffusion problem is discussed by Carslaw and Jaeger's [1], whose book includes analytical solutions and Green's Functions for the heat transfer equation. Different techniques can be used to evaluate the transient heat diffusion. They are frequently grouped by the form they adopt the time-dependent terms: the "time marching" scheme evaluates the solution at successive time intervals starting from a specified initial condition; the Laplace transform converts the time domain diffusion equation into an elliptical equation.

In order to deal with anisotropic and inhomogeneous media different numerical methods have been developed to analyse the heat transfer, such as the Finite Elements [2], the Finite Differences [3] and the Boundary Elements Method (BEM). A distinctive feature of the BEM is that the entire domain does not need to be discretized, yet a fully populated system of equations is achieved instead of the sparse system provided by the Finite Element and Finite Difference techniques. Since BEM only needs the discretization of the boundary interfaces between different media the computational effort is reduced. The Boundary Element Method has already been used in the "time marching" approaches. Chang et al. [4] proposed the first time-domain direct boundary integral method to study planar transient heat conduction. Wrobel and Brebbia [5] also used a BEM formulation for axisymmetric diffusion

problems. Dargush and Banerjee [6] proposed a BEM approach in the time domain, where planar, three-dimensional and axisymmetric analyses are all addressed with a time-domain convolution.

In this work, the transient heat transfer is computed by means of a different approach from those described above. In the BEM model proposed, the calculations are first computed in the frequency domain. The time series are found by applying an (fast) inverse Fourier transform into space-time. The unsteady-state heat transfer is calculated in a solid layer that may contain inclusions, and is bounded by two semi-infinite media. This system can be subjected to a three-dimensional heat source placed within or outside the panel. Both conduction and convection are considered. The full discretization of the flat solid interfaces of the layered system can be avoided by incorporating the analytical solutions known for this formation. So, only the boundary of the inclusions inside this solid layer needs to be discretized.

Problem formulation

The diffusion equation for transient heat transfer by conduction and convection is modified applying a Fourier transformation in the time domain. Thus, the problem is approached in the frequency domain.

The analysis of 3D problems can be computationally demanding. If the geometry of the media does not vary along one direction (z) the 3D solution is best expressed as a summation of 2D solutions. This is done by applying a Fourier transform along that direction (Tadeu & Kausel [6]). Each 2D problem is computed for a different spatial wavenumber k_z .

The fundamental solution of the 2D equation in the frequency domain can be written as a discrete summation of heat plane waves following an approach similar to the one used first by Lamb [8] for the propagation of elastodynamic waves in 2D media, and then by other authors such as Bouchon [9] and Tadeu et al. [10] to compute 3D elastodynamic fields using a discrete wave number representation. The discrete summation is achieved assuming the existence of an infinite number of virtual sources distributed along the x direction, at equal intervals L_x . For a solid full space it can be written as

$$\tilde{T}_j(\omega, x, y, k_z) = E_0 \frac{V_x(y-y_0) + V_y(y-y_0) + V_z(y-y_0)}{2K} \sum_{n=-\infty}^{n=+\infty} \left(\frac{E}{v_n} \right) E_d \quad (1)$$

in which V_x , V_y and V_z are the velocity components in the direction x , y and z respectively, ω is the frequency, T is the temperature, $E_0 = -i/2kL_x$, $E = e^{-iv_n|y-y_0|}$, $E_d = e^{-ik_x(x-x_0)}$, $v_n = \sqrt{-((V_x + V_y + V_z)/2K)^2 - i\omega/K - k_z^2 - k_{xn}^2}$ with $(\text{Im}(v_n) \leq 0)$ and $k_{xn} = 2\pi n/L_x$. This summation can be approximated by a finite sum of terms (N).

The solution in the spatial-temporal domain is computed by applying inverse fast Fourier transforms in k_z and in the frequency domain.

The Green's functions for transient heat conduction through a solid layer with thickness h , bounded by two semi-infinite solid media, are established assuming that convection and conduction are involved. The response is computed as the sum of the source terms (the incident field) equal to those in the full-space and the surface terms (surface heat waves generated in the two solid interfaces (1,2)) needed to satisfy the continuity of temperature and normal fluxes at the solid-solid interfaces. The surface terms can be expressed in a form similar to that of the source term.

Upper semi-infinite space (interface 1) $\tilde{T}_{02}(\omega, x, y, k_z) = E_{00} e^{\frac{V_{y0}(y-y_0)}{2K_0} \sum_{n=-\infty}^{n=+\infty} \left(\frac{E_{01}}{V_{n0}} A_{n0}^b \right)} E_d$ (2)

Solid layer (interface 1) $\tilde{T}_{11}(\omega, x, y, k_z) = E_{01} e^{\frac{V_{y1}(y-y_0)}{2K_1} \sum_{n=-\infty}^{n=+\infty} \left(\frac{E_{11}}{V_{n1}} A_{n1}^t \right)} E_d$ (3)

Solid layer (interface 2) $\tilde{T}_{12}(\omega, x, y, k_z) = E_{01} e^{\frac{V_{y1}(y-y_0)}{2K_1} \sum_{n=-\infty}^{n=+\infty} \left(\frac{E_{12}}{V_{n1}} A_{n1}^b \right)} E_d$ (4)

Lower semi-infinite space (interface 2) $\tilde{T}_{21}(\omega, x, y, k_z) = E_{02} e^{\frac{V_{y2}(y-y_0)}{2K_2} \sum_{n=-\infty}^{n=+\infty} \left(\frac{E_{21}}{V_{n2}} A_{n2}^t \right)} E_d$ (5)

where $E_{0j} = -i/2k_j L_x$, $E_{00} = e^{-iV_{y0}y}$, $E_{11} = e^{-iV_{n1}y}$, $E_{12} = e^{-iV_{n1}|y-h|}$, $E_{21} = e^{-iV_{n2}|y-h|}$ and $v_{nj} = \sqrt{-(V_{yj}/2K_j)^2 - i\omega/K_j - k_z^2 - k_{xn}^2}$ with $\text{Im}(v_{nj}) \leq 0$ ($j=1$ corresponds to the solid layer (medium 1), while $j=0$ and $j=2$ indicate the upper and lower semi-infinite solid space, respectively (medium 0, 2)). Meanwhile, $K_j = -k_j/\rho_j c_j$ is the thermal diffusivity in the solid medium j (k_j , ρ_j and c_j are the thermal conductivity, the density and the specific heat of the material in the solid medium, j , respectively).

The coefficients A_{n0}^b , A_{n1}^t , A_{n1}^b and A_{n2}^t are computed by imposing the appropriate boundary conditions, so that the field produced simultaneously by the source and surface terms leads to the continuity of heat fluxes and temperatures at $y=h$ and $y=0$.

This leads to the following system of four equations, when the heat source is placed within the solid layer.

$$\begin{bmatrix} \left[\frac{V_{y0}}{2K_0} + iV_{n0} \right] \frac{c_{30}}{c_{41}} & -\left[\frac{V_{y1}}{2K_1} - iV_{n1} \right] & -\left[\frac{V_{y1}}{2K_1} + iV_{n1} \right] e^{-iV_{n1}h} & 0 \\ \frac{k_1 c_{30}}{k_0 c_{41}} & -1 & -e^{-iV_{n1}h} & 0 \\ 0 & \left[\frac{V_{y1}}{2K_1} - iV_{n1} \right] e^{-iV_{n1}h} & \left[\frac{V_{y1}}{2K_1} + iV_{n1} \right] & -\left[\frac{V_{y2}}{2K_2} - iV_{n2} \right] \frac{c_{42}}{c_{31}} \\ 0 & e^{-iV_{n1}h} & 1 & -\frac{k_1 c_{42}}{k_2 c_{31}} \end{bmatrix} \begin{bmatrix} A_{n0}^b \\ A_{n1}^t \\ A_{n1}^b \\ A_{n2}^t \end{bmatrix} = \begin{bmatrix} b_1 \\ b_2 \\ b_3 \\ b_4 \end{bmatrix} \quad (6)$$

where $c_{3j} = \frac{1}{V_{nj}} e^{\frac{V_{yj} \left(\sum_{l=1}^j h_l - y_0 \right)}{2K_j}}$, $c_{4j} = \frac{1}{V_{nj}} e^{\frac{V_{yj} \left(\sum_{l=1}^{j-1} h_l - y_0 \right)}{2K_j}}$, while $b_1 = \left[V_{y1}/2K_1 + iV_{n1} \right] e^{-iV_{n1}y_0}$,

$b_2 = e^{-iV_{n1}y_0}$, $b_3 = -\left[V_{y1}/2K_1 - iV_{n1} \right] e^{-iV_{n1}|h-y_0|}$ and $b_4 = -e^{-iV_{n1}|h-y_0|}$ if the source is in the solid layer ($0 < y_0 < h_1$).

The temperature for the three solid media is computed by adding the contribution of the source terms to that associated with the surface terms originated at the various interfaces. This gives the following expressions for the temperatures in the three solid media, when the source is in the solid layer,

$$\tilde{T}(\omega, x, y, k_z) = E_{00} e^{\frac{V_{y0}(y-y_0)}{2K_0} \sum_{n=-\infty}^{n=+\infty} \left(\frac{E_{01}}{V_{n0}} A_{n0}^b \right)} E_d \quad \text{if } y < 0$$

$$\begin{aligned}\tilde{T}(\omega, x, y, k_z) &= \frac{-i}{4k_1} e^{\frac{V_{y1}(y-y_0)}{2K_1}} H_0(K_{r1} r_0) + E_{01} e^{\frac{V_{y1}(y-y_0)}{2K_1}} \sum_{n=-\infty}^{n=+\infty} \left(\frac{E_{11}}{V_{n1}} A'_{n1} + \frac{E_{12}}{V_{n1}} A^b_{n1} \right) E_d \quad \text{if } 0 < y < h_1 \\ \tilde{T}(\omega, x, y, k_z) &= E_{02} e^{\frac{V_{y2}(y-y_0)}{2K_2}} \sum_{n=-\infty}^{n=+\infty} \left(\frac{E_{21}}{V_{n2}} A'_{n2} \right) E_d \quad \text{if } y > h_1\end{aligned}\quad (7)$$

These solutions assumed that the spatially sinusoidal harmonic heat source is in the solid layer. However, the expressions can be easily manipulated to accommodate another source location.

The formulation used to compute the three-dimensional heat field, generated by a spatially sinusoidal harmonic heat line source, in a layered formation with buried inclusions is based on a BEM model (not described here). It incorporates the Green's functions derived above which take the presence of the solid layer interfaces into account. Therefore, only the inclusions' surface need discretization with boundary elements. This procedure contributes to a better performance of the BEM model.

Applications

The above BEM model is now used to analyze the importance of the presence of thermal heterogeneities embedded in a solid layer. The transient heat transfer through a solid layer (concrete medium) containing inclusions, buried in two semi-infinite media (water) is computed, when both conduction and convection phenomena are considered. Two different structures were modeled, assuming that three inclusions, made of either polystyrene (*Case 1*) or steel (*Case 2*), lie inside the solid layer (0.3 m thick). This system was subjected to a plane heat source placed in the lower medium ($y_0 = -0.1\text{m}$). The convection velocities (in the y direction) applied to the top and the bottom media were 2×10^{-6} m/s, 1×10^{-6} m/s, respectively.

The thermal properties of the concrete layer allow $k = 1.4 \text{ W.m}^{-1}.\text{C}^{-1}$, $c = 880 \text{ J.Kg}^{-1}.\text{C}^{-1}$ and $\rho = 2300 \text{ Kg.m}^{-3}$, while the top and bottom unbounded media take the properties of the water $k = 0.606 \text{ W.m}^{-1}.\text{C}^{-1}$, $c = 4181 \text{ J.Kg}^{-1}.\text{C}^{-1}$ and $\rho = 998 \text{ Kg.m}^{-3}$. The thermal properties of the inclusions are assumed to be $k = 0.027 \text{ W.m}^{-1}.\text{C}^{-1}$, $c = 1210 \text{ J.Kg}^{-1}.\text{C}^{-1}$ and $\rho = 55 \text{ Kg.m}^{-3}$ if they are polystyrene, while for the steel heterogeneities they are $k = 63.9 \text{ W.m}^{-1}.\text{C}^{-1}$, $c = 434 \text{ J.Kg}^{-1}.\text{C}^{-1}$ and $\rho = 7832 \text{ Kg.m}^{-3}$.

All the computations are performed for 128 frequencies assuming a frequency increment of $0.5e^{-5}$ Hz, which gives a frequency range of $[0, 64e^{-5} \text{ Hz}]$. The total duration of the time domain results is 55.56 h.

Initial conditions of null temperatures in the full domain are assumed. The heat plane source placed at $y_0 = -0.1\text{m}$ starts emitting energy at $t \approx 0.76$ h and its power is increased linearly from 0.0 W to 1000.0 W, reaching maximum power at $t \approx 3.46$ h. This value is maintained for a period of $t \approx 2.72$ h. The power then falls linearly to 0.0 W, which occurs at $t \approx 8.89$ h. Assuming this energy power, the temperature evolution was computed at a grid of receivers.

Fig. 1 gives two snapshots ($t = 10$ h and $t = 20$ h) showing the temperature distribution along the system, considering two cases; circular inclusions of polystyrene (*Case 1*), and steel (*Case 2*). At time $t = 10$ h the source is no longer emitting, and the energy is still propagating through the domain.

The heterogeneities introduce marked differences between the two models. The temperature distribution reveals that the steel inclusions allow a fast propagation

across them, due to the material's high diffusivity, while the polystyrene heterogeneities offer a considerable resistance to the heat transfer, due to their low conductivity coefficient. The temperature at the receivers behind the polystyrene inclusions (opposite source side) is consequently lower than in their vicinity, for the same y coordinate, while in the *Case 2* the opposite behavior is found. Comparison of the temperature distribution across the inclusions in *Case 1* and *Case 2* shows that a pronounced thermal gradient inside the polystyrene inclusion, while inside the steel inclusions the temperature variation is approximately null.

The heterogeneities' presence means that, for the upper medium, higher temperatures are first achieved in *Case 2*. At time $t = 20$ h the temperatures registered at the grid of receivers inside the solid layer (including inclusions) and in the top semi-infinite medium are still increasing, while the temperature at receivers closer to the source has clearly dropped. The behavior is maintained in both cases, since higher temperatures furthest away from the source are registered where there is a steel inclusion. Comparing the results in Fig. 1 with those computed without the positive convection velocities (not included here) – considering only the conduction phenomenon – we observe that without convection the energy takes longer to reach the slab layer and the top media, as expected.

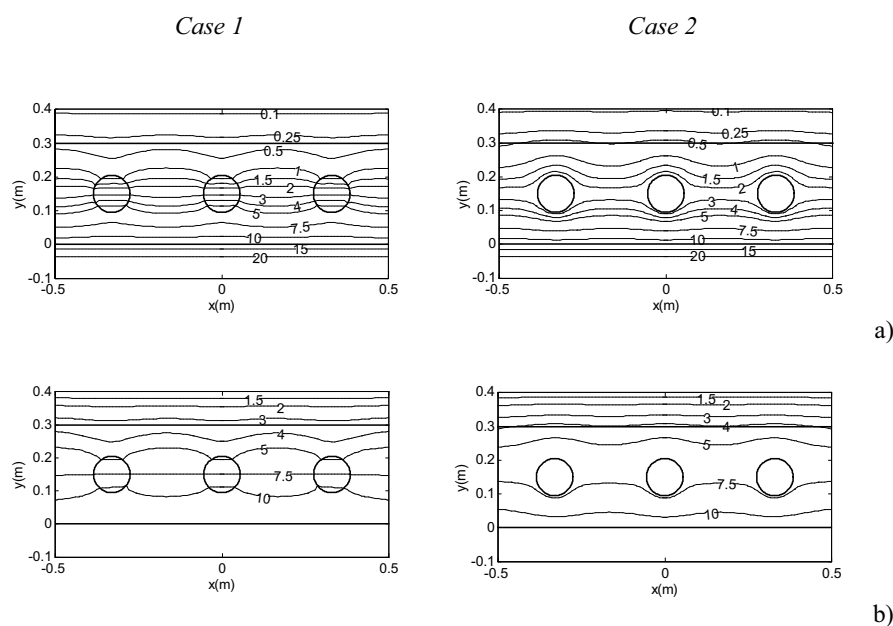


Figure 1: Distribution of temperature registered at a grid of receivers for a homogeneous concrete layer with circular inclusions of polystyrene (*Case 1*) and steel (*Case 2*): a) $t = 10$ h ; b) $t = 20$ h .

Conclusion

This paper has studied transient heat transfer by conduction and convection across a solid layer with heterogeneities, bounded by two semi-infinite media. The numerical method proposed to deal with this problem is based on a BEM formulation, and this model was used to evaluate the evolution of temperature distribution through a solid layer containing inclusions with different thermal properties when subjected to a heat

plane source. The proposed formulation incorporates the Green's functions for a layered formation. These solutions, described in the paper, are of intrinsic interest, and are also useful if incorporated in a BEM approach, allowing the calculation of the heat propagation in a layered system containing thermal heterogeneities. This combination avoids the discretization of the flat slab interfaces, contributing to the efficiency of the BEM model.

The results computed for different thermal heterogeneities show their importance to the models. The temperature distribution evolution depends on the inclusions' thermal properties and on whether convection velocity is assumed.

References

- [1] H.S. Carslaw and J.C. Jaeger, *Conduction of Heat in Solids*, second edition, Oxford University Press (1959).
- [2] K.J. Bathe, *Numerical Methods in Finite Element Analysis*, New Jersey: Prentice-Hall (1976).
- [3] V.P. Freitas, V. Abrantes and P. Crausse, Moisture Migration in Building Walls. *Analysis of the Interface Phenomena, Building and Environment*, **31**, 99-108 (1996).
- [4] Y.P. Chang, C. S.Kang and D. J.Chen, The Use of Fundamental Green's Functions for Solution of Problems of Heat Conduction in Anisotropic Media, *International Journal of Heat and Mass Transfer*, **16**, 1905-1918 (1973).
- [5] L.C. Wrobel and C.A. Brebbia, A Formulation of the Boundary Element Method for Axisymmetric Transient Heat Conduction, *International Journal of Heat and Mass Transfer*, **24**, 843-850 (1981).
- [6] G.F. Dargush and P.K. Banerjee, Application of the Boundary Element Method to Transient Heat Conduction, *International Journal for Numerical Methods in Engineering*, **31**, pp. 1231-1247 (1991).
- [7] A. Tadeu and E. Kausel, Green's functions for two-and-a-half dimensional elastodynamic problems, *Journal of Engineering Mechanics*, ASCE **126**, 1093-1097 (2000).
- [8] H. Lamb, On the propagation of tremors at the surface of an elastic solid, *Phil. Trans. Roy. Soc. London*, **A203**, 1-42 (1904).
- [9] M. Bouchon, Discrete wave number representation of elastic wave fields in three-space dimensions, *Journal of Geophysical Research*, **84**, 3609-3614 (1979).
- [10] A. Tadeu and J. António, 2.5D Green's Functions for Elastodynamic Problems in Layered Acoustic and Elastic Formations, *Journal of Computer Modeling in Engineering and Sciences*, CMES, **2**, 477-495 (2001).

The Determination of the Thermal Properties of a Homogeneous Heat Conductor

D. Lesnic

Department of Applied Mathematics, University of Leeds, Leeds LS2 9JT, UK,
amt5ld@maths.leeds.ac.uk

Keywords: Boundary Element Method, Inverse Problem, Thermal Properties.

Abstract. The aim of this paper is to determine the two constant parameters corresponding to the physical properties of a homogeneous heat conductor, namely, the heat capacity and the thermal conductivity, from heat flux and temperature measurements. An iterative nonlinear least-squares boundary element method is proposed. The inversion is performed for both exact and noisy measurements. It is shown that the thermal properties can uniquely and stably be retrieved from two measurements containing at least one heat flux measurement.

1. Introduction

The problem of determining unknown parameters in heat conduction has been treated previously in some detail [1]. Usually, these problems involve the determination of a single parameter from overspecified boundary data. In some applications, however, it is desirable to determine more than one parameter [2]. Consider for example, the one-dimensional conduction of heat in a homogeneous medium of finite length. Previously, it has been shown that using certain experiments the thermal conductivity and the heat capacity of a homogeneous heat conductor can uniquely be determined from a single measurement (at two instants) of the heat flux at the boundary [3]. In these studies, the determination of the two coefficients is accomplished by means of an intersecting graph technique [2]. However, this method is restricted to the identification of only two parameters and cannot easily be extended to more than two unknowns. Therefore, in this paper a numerical method is proposed in order to overcome this restriction. Moreover, inverse formulations which allow for temperature measurements are also investigated.

2. Inverse Problem Formulation

We consider a homogeneous finite slab heat conductor of length $L > 0$ initially at a uniform temperature. The upstream face of the sample $x = 0$ is heated, whilst the downstream face $x = L$ is kept insulated. We can then formulate the inverse problem of determining a pair of positive constants (C, K) and a function $T \in C^1([0, L] \times [0, t_f]) \cap C^2((0, L) \times (0, t_f))$ such that

$$\begin{aligned} C \frac{\partial T}{\partial t}(x, t) &= K \frac{\partial^2 T}{\partial x^2}(x, t), & (x, t) &\in (0, L) \times (0, t_s) \\ T(x, 0) &= 0, & x &\in (0, L) \\ T(0, t) &= f(t), & t &\in (0, t_s) \\ \frac{\partial T}{\partial x}(L, t) &= 0, & t &\in (0, t_s) \end{aligned} \quad (1)$$

plus any two of the following additional boundary measurements

$$\begin{aligned} (a) \quad -K \frac{\partial T}{\partial x}(0, \bar{t}_1) &= q_1, & (b) \quad -K \frac{\partial T}{\partial x}(0, \bar{t}_2) &= q_2 \\ (c) \quad T(L, \bar{t}_1) &= T_1, & (d) \quad T(L, \bar{t}_2) &= T_2 \end{aligned} \quad (2)$$

where $0 < \bar{t}_1 < \bar{t}_2 \leq t_s$ are given instants, f is a strictly monotone increasing continuously differentiable given function satisfying $f(0) = 0$, and $q_1 > 0$, $q_2 > 0$, T_1 and T_2 are given numbers. In eqs (1), T represents the temperature, and C and K are the heat capacity and thermal conductivity of the heat conductor, respectively. For the analysis performed in this study it is not necessary that the times at which we record the heat flux (2a,2b) and the temperature (2c,2d) measurements be the same. Also, temperature measurements at internal locations (x_i, \bar{t}_i) , $i = 1, 2$, with $0 < x_1 \leq x_2 < L$, may replace the boundary temperature measurements (2c,2d).

The case of a single unknown parameter $\alpha = K/C$ representing the thermal diffusivity of the heat conductor has been treated previously in [4]; however, in some situations, it is desirable to determine both C and K . Using the Green function for the initial boundary value formulation (1), it can be shown that the solution (C, K, T) of the inverse problem given by eqs (1), (2a) and (2b) is unique [3]. In the next sections we develop an iterative nonlinear least-squares boundary element method for the numerical solutions of the inverse problems given by eqs (1) and any two of the eqs (2a-2d).

2.1. The Boundary Element Method

The boundary integral equation associated to eqs (1) is given by

$$0.5 T(x, t) = \int_0^t \alpha \left[f(t') \frac{\partial F}{\partial x'}(x, t; 0, t') - T(L, t') \frac{\partial F}{\partial x'}(x, t; L, t') - F(x, t; 0, t') \frac{\partial T}{\partial x'}(0, t') \right] dt', \quad t \in [0, t_s], x \in \{0, L\} \quad (3)$$

where F is the fundamental solution for the one-dimensional heat eq (1)₁ which is given by

$$F(x, t; x', t') = \frac{H(t - t')}{2\sqrt{\pi\alpha(t - t')}} \exp\left(-\frac{(x - x')^2}{4\alpha(t - t')}\right) \quad (4)$$

where H is the Heaviside function.

The boundary element method (BEM) employed in this study is based on the numerical discretisation of eq (3) using N constant uniform boundary elements on the whole time interval $[0, t_s]$ at each of the boundaries $x = 0$ and $x = L$, and analytical integration of the resulting integrals [5].

2.2. Numerical Results and Discussion

We consider the same typical example investigated in [3] using a graphical intersecting finite-difference technique, and therefore we take $L = 1$, $f(t) = t$, $t_s = 12$, $\bar{t}_1 = 2$ and $\bar{t}_2 = 10$. The data q_1 , q_2 , T_1 and T_2 in eq (2) is generated by solving the direct mixed well-posed problem given by eqs (1) in which $C = 0.7$ and $K = 0.2$ are assumed to be known.

Table 1 presents the numerical values of q_1 , q_2 , T_1 and T_2 obtained using the BEM for solving the boundary integral eq (3) with various numbers of boundary elements $N \in \{123, 243, 483\}$. These boundary discretisations were chosen in order to ensure that the time measurement locations $\bar{t}_1 = 2$ and $\bar{t}_2 = 10$ coincide with two of the boundary element midpoint nodes. From Table 1 it can be

Table 1: The numerical values of q_1 , q_2 , T_1 and T_2 obtained using the BEM with various numbers of boundary elements $N \in \{123, 243, 483\}$.

	$N = 123$	$N = 243$	$N = 483$
q_1	0.56159	0.56151	0.56148
q_2	0.69952	0.69951	0.69950
T_1	0.69059	0.69082	0.69091
T_2	8.25155	8.25156	8.25146

seen that the numerical solution is convergent as the number of boundary elements N increases. Also it can be concluded that a mesh discretisation with $N \geq 123$ elements is sufficiently fine to ensure that any further decrease in this mesh size does not significantly affect the accuracy of the numerical results. The mesh size $N = 123$ is therefore kept fixed in the inverse analysis which is performed in the next subsection.

2.2.1. Inverse Analysis

Once the values of q_1 , q_2 , T_1 and T_2 have been obtained accurately, any two of them can then be used as input data in eqs (2a-2d) in the inverse analysis of determining the thermal property coefficients C and K and the temperature solution T inside the domain.

For inversion we minimize the nonlinear least-squares function

$$S(C, K) := \lambda_1 | q_1 - (-K^c T_x^c(0, \bar{t}_1)) |^2 + \lambda_2 | q_2 - (-K^c T_x^c(0, \bar{t}_2)) |^2 + \lambda_3 | T_1 - T^c(L, \bar{t}_1) |^2 + \lambda_4 | T_2 - T^c(L, \bar{t}_2) |^2 \quad (5)$$

where $T_x = \partial T / \partial x$, and the superscript c stands for the numerically calculated quantities from iteratively solving using the BEM the mixed direct problem (1).

In expression (6), the constants λ_i for $i = \overline{1, 4}$, are chosen zero if we do not measure the corresponding quantity with which they are multiplied, and $\lambda_i = 1$ for $i = \overline{1, 3}$, $\lambda_4 = 10^{-2}$ otherwise. The value of 10^{-2} instead of unity for λ_4 was included for scaling purposes only, because of the different order of magnitudes of the measurements q_1 , q_2 , T_1 and T_2 shown in Table 1 for the example considered. Based on this discussion we distinguish six inverse problem formulations given by eqs (1) together with either of the following additional data:

- (i) eqs (2a) and (2b), i.e. $\lambda_1 = \lambda_2 = 1$, $\lambda_3 = \lambda_4 = 0$;
- (ii) eqs (2a) and (2c), i.e. $\lambda_1 = \lambda_3 = 1$, $\lambda_2 = \lambda_4 = 0$;
- (iii) eqs (2a) and (2d), i.e. $\lambda_1 = 1$, $\lambda_4 = 10^{-2}$, $\lambda_2 = \lambda_3 = 0$;
- (iv) eqs (2b) and (2c), i.e. $\lambda_2 = \lambda_3 = 1$, $\lambda_1 = \lambda_4 = 0$;
- (v) eqs (2b) and (2d), i.e. $\lambda_2 = 1$, $\lambda_4 = 10^{-2}$, $\lambda_1 = \lambda_3 = 0$;
- (vi) eqs (2c) and (2d), i.e. $\lambda_3 = 1$, $\lambda_4 = 10^{-2}$, $\lambda_1 = \lambda_2 = 0$.

The inverse formulation (vi) given by eqs (1), (2c) and (2d) involve only the thermal diffusivity parameter $\alpha = K/C$, and therefore in this case we can retrieve only α . In contrast, all the inverse formulations (i)-(v) contain both C and K since always a flux measurement given by eq (2a) or (2b) is taken into account, and in these situations we expect both parameters K and C to be retrieved.

For the minimization of the function S we employ a constrained minimization procedure given by the NAG routine E04UCF. The constraints that the solution (C, K) should be positive and finite are numerically implemented by taking the lower bound as a very small positive number such as $m_i = 10^{-10}$ and the upper bound as a very large number such as $M_i = 10^{10}$, $i = 1, 2$.

The gradient of the least-squares function (6) has been calculated using forward finite differences with a step size h . For the accurate evaluation of the gradient ∇S , the NAG routine E04UCF employed requires the use of $h = 10^{-3}$ for the formulations (i) and (v), $h = 10^{-4}$ for the formulation (iii), and $h = 10^{-5}$ for the formulations (ii), (iv) and (vi).

An arbitrary initial guess $(C_0, K_0) = (1, 1)$ was chosen. Several other guesses were considered and it was found that the numerical results did not differ significantly for all the formulations (i)-(v), and this shows that the constrained minimization approach proposed is robust. In the formulation (vi) different initial guesses gave different values for the retrieved coefficients K and C , however the retrieval of the ratio $\alpha = K/C$ was found to be independent of the initial guess.

The stability of the numerical solution has been investigated by introducing noise in the measured data given by eqs (2a-2d) using the truncated values $q_1^{(n)} = 0.56$, $q_2^{(n)} = 0.69$, $T_1^{(n)} = 0.69$ and $T_2^{(n)} = 8.2$, see Table 1 for $N = 123$, as well as by perturbing the temperature function $f(t)$ using $p\%$ noisy data, i.e.

$$f^\epsilon(\tilde{t}_i) := f(\tilde{t}_i) + \epsilon_i = \tilde{t}_i + \epsilon_i, \quad i = \overline{1, N} \quad (6)$$

where ϵ_i are Gaussian random variables with mean zero and standard deviations $\sigma_i = p | f(\tilde{t}_i) | / 100 = p \tilde{t}_i / 100$, generated using the NAG routine G05DDF.

The optimal solution has been reached within 15 iterations in the formulation (i), 8 iterations in the formulations (ii) and (v), 10 iterations in the formulations (iii) and (iv), and 4 iterations in the formulation (vi).

Table 2 shows the numerical retrieved values of C and K for the formulations (i)-(vi) obtained when both exact and noisy data are inverted. The numerically obtained optimal minimum values of

Table 2: The numerically retrieved values of C and K for the formulations (i)-(vi) obtained when exact data q_1, q_2, T_1, T_2 and $f(t)$ (represented by the superscript $*$), exact data $f(t)$ but noisy data $q_1^{(n)} = 0.56, q_2^{(n)} = 0.69, T_1^{(n)} = 0.69, T_2^{(n)} = 8.2$ (represented by the superscript \diamond), exact data q_1, q_2, T_1, T_2 but $p\% = 1\%$ noisy data f^ϵ (represented by the superscript b), and full noisy data $q_1^{(n)} = 0.56, q_2^{(n)} = 0.69, T_1^{(n)} = 0.69, T_2^{(n)} = 8.2$ and $p\% = 1\%$ noisy data f^ϵ (represented by the superscript d), are inverted.

Formulation	C	K	$S(C, K)$	CPU
(i)	0.6999	0.1999	$1.7E - 19$	249 $*$
	0.6903	0.2036	$2.6E - 19$	223 \diamond
	0.6962	0.1989	$2.9E - 18$	258 b
	0.6866	0.2025	$4.3E - 18$	230 d
(ii)	0.6999	0.1999	$2.6E - 21$	117 $*$
	0.6982	0.1993	$4.4E - 21$	117 \diamond
	0.6975	0.1982	$7.0E - 22$	117 b
	0.6957	0.1975	$1.4E - 18$	117 d
(iii)	0.6999	0.1999	$5.3E - 17$	178 $*$
	0.7052	0.1956	$1.8E - 22$	179 \diamond
	0.7024	0.1957	$2.0E - 18$	179 b
	0.7075	0.1916	$6.6E - 18$	179 d
(iv)	0.6999	0.1999	$2.2E - 20$	144 $*$
	0.6904	0.1971	$3.4E - 22$	143 \diamond
	0.6962	0.1978	$1.1E - 20$	144 b
	0.6868	0.1950	$1.2E - 23$	144 d
(v)	0.6999	0.1999	$4.0E - 17$	222 $*$
	0.6905	0.1916	$2.1E - 16$	222 \diamond
	0.6963	0.1940	$1.0E - 16$	222 b
	0.6870	0.1860	$2.5E - 16$	223 d
(vi)	1.5440	0.4411	$1.9E - 18$	49 $*$
	1.5449	0.4402	$2.3E - 5$	49 \diamond
	1.5460	0.4388	$1.1E - 5$	49 b
	1.5470	0.4379	$6.7E - 5$	49 d

the least-squares function S and the CPU time (in seconds) are also included. From Table 2 it can be seen that in all the inverse formulations (i)-(v) accurate and stable approximations to the exact solution $(C, K) = (0.7, 0.2)$ are obtained, whilst in the inverse formulation (vi), as expected, only the thermal diffusivity $\alpha = 0.2/0.7 \approx 0.28571$ can be retrieved.

3. Conclusions

In this paper the determination of the constant thermal properties of a homogeneous finite slab heat conductor has been accomplished from a heat transfer experiment in which a rod, initially at a uniform temperature, is increasing heated smoothly at one side, whilst the other side is kept insulated. It is shown that both the heat capacity and the thermal conductivity of the conductor can uniquely and stably be determined by measuring the heat flux at the heated face of the sample at two different instants, or by measuring the heat flux at a single instant together with one temperature measurement at a sensor located within or at the insulated side of the sample. If only temperature measurements are recorded then only the thermal diffusivity of the heat conductor can be determined. The numerical analysis is based on an iterative nonlinear least-squares BEM. The numerically obtained results for both exact and noisy data show that the numerical solution is convergent, accurate and stable. Furthermore, the numerical method proposed in this study can easily be extended to inhomogeneous

initial and boundary conditions and to higher dimensions.

Acknowledgement

The author would like to acknowledge some funding support received from the UK Royal Society.

References

- [1] G. Anger, *Inverse Problems in Differential Equations*, Plenum Press, New York (1990).
- [2] J.R. Cannon, P.C. DuChateau and D.L. Filmer, *Math. Biosciences* **9**, 61-70 (1970).
- [3] J.R. Cannon and P.C. DuChateau, *Int. J. Engng. Sci.*, **11**, 783-794 (1973).
- [4] J.R. Cannon, *J. Math. Anal. Appl.* **8**, 188-201 (1964).
- [5] C.A. Brebbia, J.C.F. Telles and L.C. Wrobel, *Boundary Element Techniques: Theory and Application in Engineering*, Springer-Verlag, Berlin (1984).

Near-Boundary Heat Transfer Using a Self-Regular Boundary Element Method Formulation

Ariosto B. Jorge¹, Paulo A. C. Porto¹ and Gabriel O. Ribeiro²

¹ Institute of Mechanical Engineering, UNIFEI - Federal University of Itajubá, Av BPS, 1303, Itajubá, MG, Brazil - CEP 37500-000. Email: ariosto.b.jorge@unifei.edu.br

² Department of Structural Engineering, UFMG Federal University of Minas Gerais, Av do Contorno, 842 - 2o andar, Belo Horizonte, MG, Brazil - CEP 30110-060. Email: gabriel@dees.ufmg.br

Keywords: BIE - Boundary Integral Equations, BEM - Boundary Element Methods, Self-Regular Formulations, Potential Theory, Near-Boundary Heat Transfer.

Abstract. Accurate assessment of near-boundary thermal fields is crucial in many emerging heat transfer applications, such as rapid laser machining and electro-thermal simulation of semiconductor devices, that require the resolution of disparate length scales between the overall system boundaries and the local regions of interest. Computational approaches that employ domain discretization rely on approximate interpolation between coarse nodal points or ultra-refined meshes to resolve the requisite length scales within the domain. Boundary element methods offer an advantage over domain-discretization approaches due to their continuous description of interior fields. However, traditional boundary element methods suffer from inaccuracy near domain boundaries as a result of quasi-singular integrals between the domain point and nearby boundary nodes. The present work reports the results of a self-regular boundary element method (BEM) that eliminates these singularities. The method of computation favorably addresses the physical scaling problems encountered in modeling problems with length scales ranging from centimeters to nanometers. The self-regular BEM, which recently has been applied to potential theory, overcomes many of the problems associated with traditional boundary integral methods. In particular, the new formulation eliminates the need to evaluate the singular and nearly singular integrals that are traditionally required to compute fields on and very near domain boundaries. These singular integrals are the primary sources of error (particularly for near-boundary fields) in traditional BEMs. The proposed method also retains the advantages of traditional BEMs in that interior (i.e., domain) fields are continuous (and postprocessed), as opposed to discretized (and part of the solution matrix). The foregoing factors-interior domain field continuity and near-boundary accuracy-make the proposed formulation ideal for treating length-scale issues encountered in the thermal analysis near-boundary regions.

Introduction

The problem of heat conduction of small electronic components - microscale or even nanoscale - may pose difficulties for its numerical solution due to scaling problems. One dimension of the domain being evaluated may be much smaller than the other, so the solution for any interior point in the domain is in fact a near-boundary heat transfer problem.

Another near-boundary heat transfer problem arises in the evaluation of the potential field at interior points close to some point in the domain with a locally concentrated heat source. The heat source could be a laser beam aimed at this point. A domain point source could be interpreted as a singularity in the potential field at the point source. So, the source can be written as $Q_D * \delta(y, X_D)$, where Q_D is the magnitude of a domain source located at the point X_D and $\delta(y, X_D)$ is the Dirac Delta function. For an interior point $y \neq X_D$, then $\delta(y, X_D) = 0$, and the potential field is continuous. For domain points approaching the source point where the singularity is concentrated, numerical difficulties may arise when evaluating the potential field. The singular point is out of the domain where the potential is defined, so the solution for the potential field at interior points in the vicinity of the point source is also seen as a near-boundary heat transfer problem.

These two problems could appear combined. In this case, if the domain has one dimension that is much smaller than the other, then the domain point source will be located very close to some part of the boundary, and this would represent a quasi-singularity in the boundary solution at a boundary points close to this domains point source.

Among the methods to solve this kind of conduction problem, three can be cited: the finite element method (FEM), the expansion as an infinite sum of eigenfunctions and the boundary element method (BEM).

The finite element method can be seen as obtained from the minimization of a certain functional. The FEM solution in a certain element is approximate, and corresponds to “average” nodal values that will be part of the total solution for the minimization problem. This FEM solution “damps” the singular behavior and requires highly-refined meshes in a region around the singularity to obtain a better approximation of the singular behavior. Also, finite element methods usually do not work well for domain point sources. The FE method usually will have to assume an approximation for the point source as if it were in fact distributed over a small domain around the point source. So, the FEM solution is inaccurate in a region close to the domain point source due to this approximation.

Solutions based on infinite sum of eigenfunctions can be written for the potential field, assuming that this field satisfies certain continuity requirements. Examples of these solutions are the Fourier series or the infinite sum obtained using the method of integral transform [1]. For a numerical solution, the infinite sum will have to be truncated at a finite number of terms. The truncation introduces an error in the solution. This error may be small at an interior point far away from the boundary, but may increase considerably when approaching the boundary. The near boundary solution may also oscillate, due to the Gibbs phenomenon, and is not accurate too.

The boundary element method appears as the optimal approach when an accurate solution is needed either close to the boundary, or close to the domain source, or both. The method relies on the use of Green’s Second Identity, for potential problems, which is an exact equation. Differently from FEM, there is no approximation in the formulation of the boundary integral equation (BIE) related to the problem. The only approximation comes in the process of discretizing the BIE to obtain the BEM. One of the approaches to obtain a system of equations is the direct BEM, that uses the collocation method. The solution will be evaluated at a certain number of collocation boundary points. Performing numerical integrations over all boundary elements when collocation at a boundary point (usually, a node) generates a row of the system of equations. The integration process includes also the element where the collocation point is, and the kernel of the boundary integral will be singular at the moment when the collocation point and the integration point (known as the field point) coincide. The integrals in the BIE may be singular or weakly-singular. The weakly-singular integral may be evaluated numerically using special techniques, such as logarithmic quadrature. But the singular integral exists only in the Cauchy Principal Value (CPV) sense. There are two approaches to integrate the singular integral.

The first approach is the standard formulation in which the CPV terms are evaluated either analytically or in an indirect manner [2]. The second approach is to regularize the singular integral before performing the numerical integration. The integral is “self-regular” as it describes a problem that is regular in nature. In the work of Cruse and co-workers [3, 4], two self-regular integral equations were obtained: the “potential-BIE”, obtained from the regularization of the CPV formulation for the potential, and the “flux-BIE”, obtained from the regularization of the gradient of the original equation, projected in the normal direction. Several approaches for regularization can be found in the literature, for various problems, such as potential, elasticity and fracture mechanics [5, 6, 7, 8, 9]. In the case of the quasi-singularities on the boundary solution, arising from the fact that the domain point source is located very close to some part of the boundary, the “regular” character of the self-regular formulations points them out as the natural choice for a BEM formulation. The self-regular formulations are expected to be more robust with regard to these quasi-singularities.

BEM formulations including domain sources

The standard CPV formulation for the potential $T(x)$ can be written in 2-D as [2]

$$2\pi C(x)T(x) + \int_{\partial\Omega} T(Q) \frac{\partial}{\partial n} \ln \left(\frac{1}{r(Q,x)} \right) dS(Q) = \\ + \int_{\partial\Omega} \frac{\partial}{\partial n} T(Q) \ln \left(\frac{1}{r(Q,x)} \right) dS(Q) - \int_{\Omega} \ln \left(\frac{1}{r(p,x)} \right) b(p) dV(p) \quad (1)$$

where in the case of N_D domain point sources the integral on the domain Ω is just the sum of the value of each magnitude Q_D times the fundamental solution at point $p = P_D$: $\sum_{I=1}^{N_D} Q_D(I) \ln(1/r(P_D(I), x))$. Also, $2\pi C(x)$ is the internal angle at point x . So, $C(x) = 1$ for $x \in \Omega$ and $C(x) = 1/2$ if x is a smooth point on the boundary.

The self-regular formulations for the potential problem [3, 4] can also be written including the domain integral relative to the point sources. For $x \rightarrow P \in \partial\Omega$ the self-regular potential-BIE is

$$0 = - \int_{\partial\Omega} [T(Q) - T(P)] \frac{\partial}{\partial n} \ln \left(\frac{1}{r(Q, P)} \right) dS(Q) + \int_{\partial\Omega} \frac{\partial}{\partial n} T(Q) \ln \left(\frac{1}{r(Q, x)} \right) dS(Q) - \sum_{I=1}^{N_D} Q_D(I) \ln \left(\frac{1}{r(P_D(I), P)} \right) \quad (2)$$

and the self-regular flux-BIE is

$$0 = n_i(P) \int_{\partial\Omega} [T(Q) - T^L(Q)] \ln \left(\frac{1}{r(Q, P)} \right)_{,ij} n_j(Q) dS(Q) - n_i(P) \int_{\partial\Omega} [\vec{\nabla} T(Q) - \vec{\nabla} T(P)] \cdot \vec{n}(Q) \ln \left(\frac{1}{r(Q, P)} \right)_{,i} dS(Q) + n_i(P) \sum_{I=1}^{N_D} Q_D(I) \vec{\nabla} \left(\ln \left(\frac{1}{r(P_D(I), P)} \right) \right) \quad (3)$$

Comparison of solution accuracy for different formulations

The solution in the domain is obtained in a post-processing procedure from the solution on the boundary. The more accurate is the boundary solution, the more accurate will be the interior point solution. Except for a small number of simple problems, the exact solution is not available, and an estimate of the local and global errors is needed, to evaluate the quality of the numerical solution.

In this work, an error indicator is adopted from the external problem formulation to assess the boundary solution accuracy. This error estimator was derived in Ref. [10] for linear elements and its use is extended in this work for quadratic elements. The error estimator is based on the fact that the accuracy in the boundary solution plays an important role on the accuracy on any interior point solution. The exterior point is treated as an interior point, considering that the error at this interior point is dependent on the accuracy of the boundary solution, especially in the boundary region closest to this point.

Thus, solutions at exterior points are evaluated using the interior points subroutine, with the external point coordinates. As the external point is not in the domain, the potential at this point should be zero. If it is not zero, this fact is an indication of error. The closer is this external point to some region of the boundary, the more this error indicator is influenced by this part of the boundary. So, by positioning this external point at a small distance with regard to an element, most of the contribution to the error will come from this element, giving a local measure of the error, i.e., the element error. In this work, a distance of 0.25 of the size of the element closer to the external point was selected [10].

In general, the boundary error information already gives a rough idea on the quality of the solution in the domain. More accurate assessments of the domain solution may be needed in a vicinity of the domain source or in a layer between the source and the boundary in the case where one dimension of the problem is very small. To assess the error in the potential at interior points in a certain region directly, procedures such as gradient recovery for the domain solution or comparison between two domain solutions based on subsequent boundary mesh refinements could be adopted.

Numerical results and discussion

To evaluate the influence of the domain sources, of the scaling factors and of the near-boundary location of the interior points in the boundary solution accuracy, a two-dimensional heat conduction problem in a square domain is considered, as shown in Fig. 1(a). The flux is prescribed on the two horizontal edges, which are insulated (zero flux), and the temperature is prescribed on the other two opposite vertical edges. The thermal conductivity is $k = 1$. In this work, quadratic elements are used, and the self-regular formulations (potential-BIE and flux-BIE) are compared with the standard CPV formulation.

This problem is adapted from [2, 4] by including a domain point source with varying magnitude at different locations on the square. When no domains sources are added, the exact solution for the potential and for the flux is known, thus allowing the exact error to be evaluated. For the problem with added domain sources, only the information from the external domain error estimator is available.

The point source was collocated at the center of the square, and then moved to the boundary through three different paths, as shown in Fig. 1(b). The first path (1-5-6-7) is described towards a boundary corner, where both discontinuities of the normal vector and of the boundary conditions occurred. The second path (1-8-9-10) moves to a smooth part of the boundary, in the middle of a side, with no discontinuities in the boundary

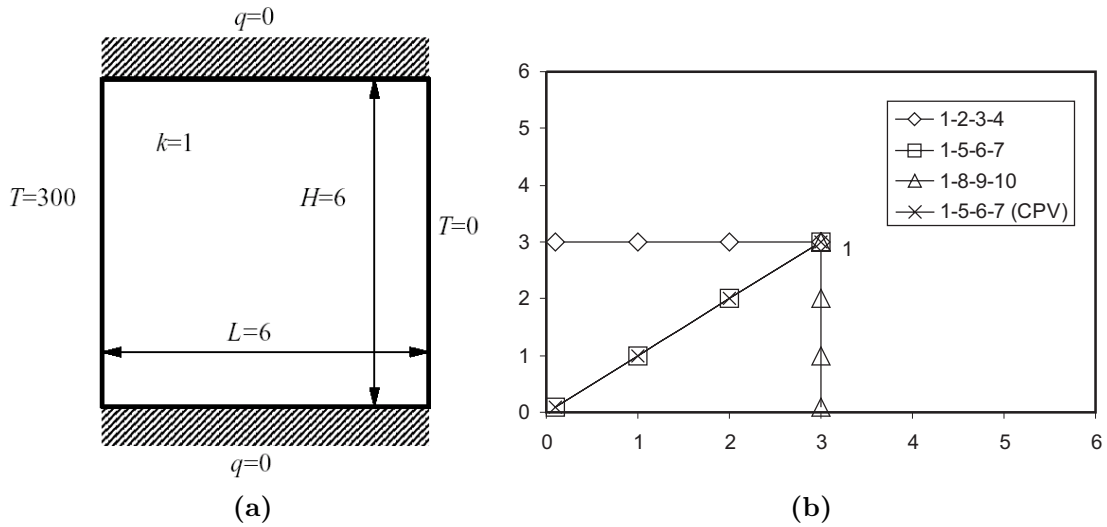


Figure 1: Example problem: heat conduction in a square domain: a) dimensions and boundary conditions; b) Path from interior to boundary.

conditions. In this case, the flux is prescribed. The third path (1-2-3-4) is directed to a smooth part of the boundary, where now the potential is prescribed.

For the three formulations evaluated – self-regular potential-BIE, self-regular flux-BIE, and standard CPV – several meshes were tested. Starting from a 16-node mesh, the other meshes were obtained in a simple h -refinement procedure, by just dividing the element size by two. This means that at every refinement, the distance between the external point, used for the error measure, and the boundary is divided by two, also. The numerical results for the average (global) error from the external formulation are shown in Fig. 2, where part (a) corresponds to the original problem, with no domain source, and part (b) corresponds to a domain source of magnitude $Q_D = 100$ added at the center of the domain.

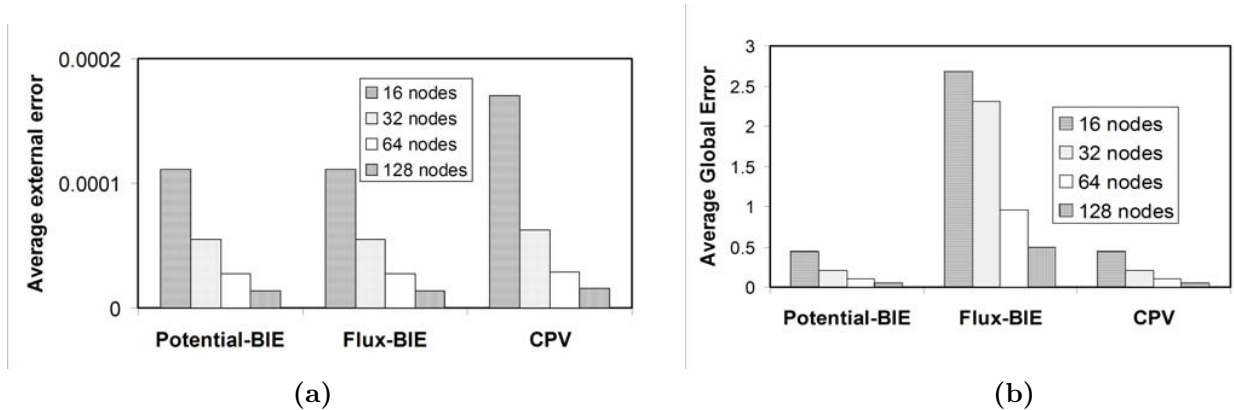


Figure 2: Global error for three formulations: self-regular Potential-BIE and Flux-BIE, and CPV: a) no domain source; b) domain source of magnitude $Q = 100$ at the center.

In all cases considered, the order of magnitude of the average (global) error estimate decreases with mesh refinement, showing that the finer mesh is acting to decrease the local error. If the exterior point (used to obtain error estimator results) were approximated to the boundary without refining the mesh, the error would increase due to the proximity to the boundary. The potential-BIE results were slightly better than the corresponding standard-CPV results for most cases, with the best results obtained for the coarse mesh, were the potential-BIE results were significantly better than the corresponding standard-CPV results.

With regard to the flux-BIE, the average error results degrade significantly when a domain source was included. It is worth noting that in Ref. [4] the flux-BIE results for quadratic elements were poorer than the corresponding results for cubic and quartic elements. The flux-BIE with cubic and quartic elements – not evaluated in this work – is expected to give more accurate results. Also, a variational formulation for the

self-regular traction-BEM formulation was recently proposed in Ref. [11], in which error results for quadratic elements improved significantly. Accurate interior point results were obtained for the elasticity problem in Ref. [12] by means of a near-boundary-point (NBP) regularization. This type of NBP regularization for the interior point could be extended for the flux-BIE, and an improvement is expected in the accuracy of the interior point solution. Work is currently under way to extend this variational formulation for potential problems, and the error results for the variational flux-BIE are expected to improve with respect to the error results presented here. In what follows, only the self-regular potential-BIE and the standard-CPV continue to be compared, the discussion with the flux-BIE being left to an upcoming work, currently in preparation.

The influence of the domain aspect ratio is evaluated by keeping constant the horizontal sides, while shrinking the vertical sides, from the original 1 : 1 ratio (square problem) to ratios up to 1 : 0.00001. For the problem discretized with 64 quadratic elements (128 nodes) and with no domain sources, the exact error (error compared with the available exact solution) in the potential in one of the horizontal sides is shown in Fig. 3, where part (a) corresponds to the self-regular potential-BIE formulation, and part (b) corresponds to the standard-CPV formulation.

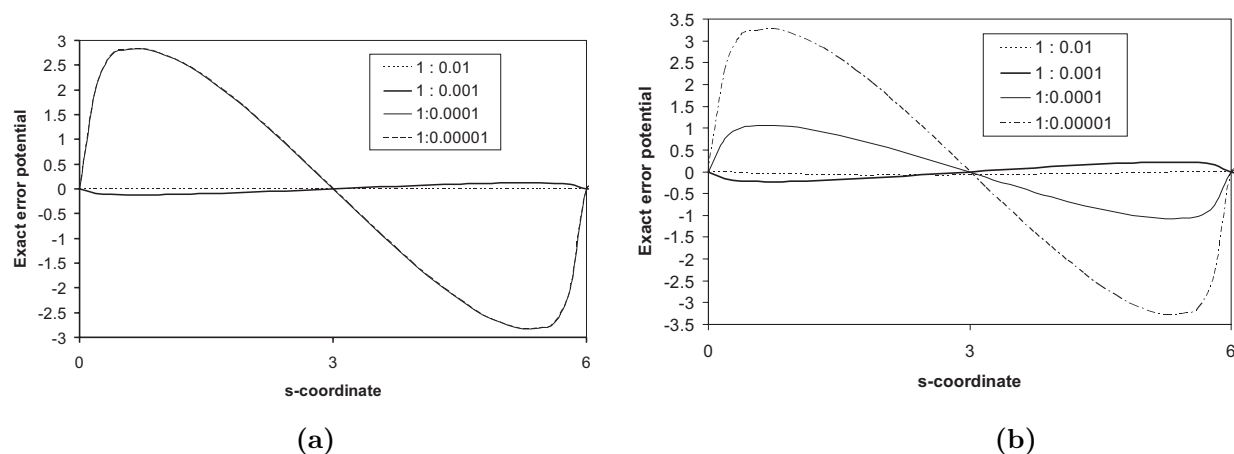


Figure 3: Influence of domain aspect ratio, without domain sources: a) Potential-BIE formulation; b) CPV formulation.

In both formulations – self-regular potential-BIE and standard-CPV – the error results increased significantly when the aspect ratio increased. For the worst case scenario (with the highest aspect ratio of 1 : 0.00001) the standard-CPV formulation gave higher values for the maximum error (maximum exact error results for the potential in the horizontal side) than the self-regular potential-BIE. Apparently, when the aspect ratio was increased, the self-regular potential-BIE error results appeared initially to degrade faster than the corresponding error results for the standard-CPV formulation, but then when the highest tested value of the aspect ratio was reached, the magnitude of the maximum error was higher in the case of the standard-CPV formulation.

The influence of the proximity to the boundary is investigated in two instances, both for the 128 node mesh, with quadratic elements. The first case corresponds to a problem with no domain source, where the exact error for the potential of the interior point is evaluated as this interior point travels towards the boundary following one of the three paths defined in Fig. 1(b). The exact error results for the self-regular potential-BIE formulation are shown in Fig. 4(a). The error results for the standard-CPV formulation are strictly similar to these results, and are not shown here. The second case corresponds to a domain source that is moved towards the boundary following one of the three above-defined paths. The average (global) error results from the external formulation are shown in Fig. 4(b) for the self-regular potential-BIE formulation. As before, the error results for the standard-CPV formulation are strictly similar to the self-regular error results. Only the CPV error for the path approaching the corner (1-5-6-7) is included in the plot.

It is worth noting in both Fig. 4 (a) and (b) the significant increase in the error (either local or global) when approaching a boundary corner, in comparison with the smallest error values when approaching smooth parts of the boundary. Highest errors were obtained both in the case where a fixed source is given (in this case, no source), and the interior point approaches the corner (exact local error, in this case), and also in the case where the domain source itself approaches the corner (average (global) error from the external formulation, in this case).

For near-boundary domain sources, locally refining the meshes in a vicinity of this point source could have an important effect on the boundary error, but this effect was not tested in this work. Also, grading the mesh

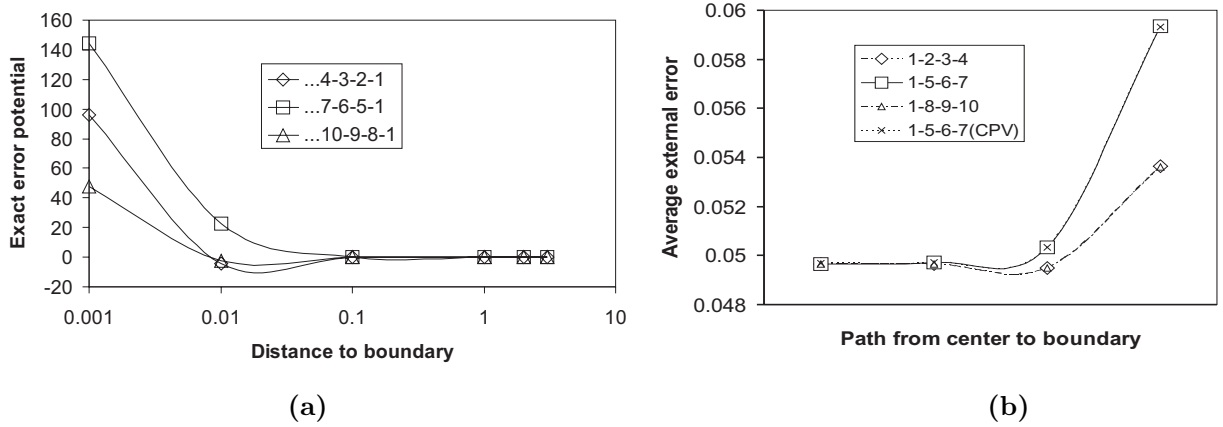


Figure 4: Near-boundary behavior of error: a) No domains sources; exact local error in potential is evaluated at interior points approaching the boundary through different paths; b) Global error from external formulation is evaluated when a domain source of magnitude $Q_D = 100$ is moved from the center to different points of the boundary.

may have an important effect on the error, in this case, as the tangential derivative of the potential may change significantly for the boundary region close to the domain source. A more detailed discussion on the influence of the tangential derivative of the potential on the boundary error can be found in reference [4].

In both formulations, standard CPV and potential-BIE, the distance of the domain point source to the boundary influences the error: the closer is the point source to the boundary, the bigger is the boundary solution error in the elements closer to the point source. Also, the numerical experiments performed indicate that there is a relation of the boundary error with respect to the boundary smoothness in a vicinity of the point source or the discontinuity in the boundary conditions in the same vicinity. In particular, highest values of the error were found when approaching a vicinity of a corner.

The scaling effect is especially important when great differences occur between the characteristic dimensions of the domain. The numerical experiments performed in this work indicate that there is a correlation between high domain aspect ratios and high error values.

Some of the results above showed a small advantage of the self-regular potential-BIE with respect to the standard CPV formulation, but on some other results no noticeable differences were found in the behavior of both the self-regular potential-BIE and the standard CPV formulations. The self-regular potential BIE has in its formulation one regularized integral and one weakly-singular integral, while the standard CPV formulation has one singular integral, evaluated in the CPV sense, and one weakly-singular integral, evaluated using the same logarithmic quadrature then in the potential-BIE. The only difference between these formulations is the evaluation of the singular integral. The equivalence between the two formulations seems to be consistent. On the other hand, the self-regular flux-BIE is expected to give better results for the error when comparing to the standard CPV formulation, as in the flux-BIE all integrals were regularized, and there are no weakly-singular integrals remaining in the final integral formulation. The study of the flux-BIE was not included in this work.

Conclusions

In this work, the influence of the aspect ratio, of the presence of domain sources and of the domain aspect ratio was demonstrated through a numerical problem. High error values were present when the aspect ratio increased, when a source was added, or when an interior point was moved towards the boundary. In this last case, a result of particular interest was that the highest error values were obtained when approaching a corner node instead of a smooth section of the boundary.

The boundary element method seems to be the most appropriate approach to deal with near-boundary heat transfer problems. Among the different BEM possibilities, the self-regular formulations are the ones that could offer more robustness with respect to the influence of the position of the point source. The potential-BIE seems to offer slightly better – or at least comparable – results than the standard CPV. The flux-BIE offers the possibility of better results for the local boundary error - yet to be confirmed by more exhaustive studies. In confirming this promise from the flux-BIE, then the self-regular BEM formulations can be considered the more

appropriate approaches to obtain a reasonable accuracy in the results for the potential in the domain, for this near-boundary heat transfer problem.

Acknowledgments

The first author would like to acknowledge the support received from CAPES - Coordenação de Aperfeiçoamento de Pessoal de Nível Superior, a Brazilian Government Agency.

References

- [1] M. N. Özisik: *Boundary Value Problems of Heat Conduction*, Dover, 1968.
- [2] C. A. Brebbia and J. Dominguez: *Boundary Elements - An Introductory Course*, Comp. Mech. Publ. - McGraw-Hill, Southampton, 1989.
- [3] T. A. Cruse and J. D. Richardson: *Self-Regularized Hypersingular BEM for Laplace's Equation*, in M. Bonnet, A. -M. Sändig and W. L. Wendland (Editors): *Mathematical Aspects of Boundary Element Methods*, Chapman & Hall / CRC, Boca Raton, FL, 2000.
- [4] A. B. Jorge, G. O. Ribeiro, T. A. Cruse and T. S. Fisher: *Self-Regular Boundary Integral Equation Formulations for Laplace's Equation in 2-D*, *Int. J. Numer. Meth. Engrg.*, 51 (1), pp. 1–29, 2001.
- [5] T. J. Rudolph: *The use of simple solutions in the regularization of hypersingular boundary integral equations*. *Mathl. Comput. Modeling*, 15, pp. 269–278, 1991.
- [6] J. D. Richardson, T. A. Cruse, and Q. Huang: *On the validity of conforming BEM algorithms for hypersingular boundary integral equations*, *Int. J. Numer. Meth. Engrg.*, 42, pp. 213–220, 1997.
- [7] V. Sladek and J. Sladek: *Singular Integrals in Boundary Element Methods*, *Advances in Boundary Elements Series*, Comp. Mech. Publ. , Southampton, 1998.
- [8] M. Bonnet: *Boundary Integral Equation Methods for Solids and Fluids*, Wiley, West Sussex, 1999.
- [9] J. Dominguez, M. P. Ariza and R. Gallego: *Flux and traction boundary elements without hypersingular or strongly singular integrals*, *Int. J. Numer. Meth. Engrg.*, 48, pp. 111–135, 2000.
- [10] A. B. Jorge, G. O. Ribeiro and T. S. Fisher: *New Approaches for Error Estimation and Adaptivity for 2-D Potential Boundary Element Methods*, *Int. J. Numer. Meth. Engrg.*, 56, pp. 117-144, 2003.
- [11] A. B. Jorge, T. A. Cruse, T. S. Fisher and G. O. Ribeiro: *A New Variational Self-Regular Traction-BEM Formulation for Inter-Element Continuity of Displacement Derivatives*, *Computational Mechanics*, 25, pp. 466–506, 2003.
- [12] J. D. Richardson and T. A. Cruse: *Weakly Singular Stress-BEM for 2D Elastostatics*, *Int. J. Numer. Meth. Engrg.*, 45, pp. 13–35, 1999.

Two-Dimensional Steady Heat Conduction Analysis of Functionally Gradient Materials by Triple-Reciprocity Boundary Element Method

Yoshihiro OCHIAI

Kinki University, Dept. of Mech. Eng., 3-4-1 Kowakae, Higash-Osaka, 577-8502, JAPAN,
ochiai@mech.kindai.ac.jp

Keywords: Boundary Element Method, Heat Conduction, Computational Mechanics, Functionally Gradient Materials

Abstract. Homogeneous heat conduction analysis can be easily solved by means of the boundary element method. However, domain integrals are generally necessary to solve the heat conduction problem in the functionally gradient materials. This paper shows that the two-dimensional heat conduction problem in the functionally gradient materials (FGM) can be solved approximately without a domain integral by the triple-reciprocity boundary element method. In this method, the distribution of domain effects is interpolated by integral equations. A new computer program is developed and applied to several problems.

Introduction

The functionally gradient material can be modeled as an inhomogeneous one in which the thermal conductivity is a continuous function of coordinates. The boundary element method is applicable to various problems of homogeneous materials. However, for inhomogeneous materials it is difficult to obtain a fundamental solution. When the analysis of heat conduction in inhomogeneous bodies is carried out using the boundary element method (BEM), generally, the domain integral due to the inhomogeneous one cannot be avoided. The conventional BEM requires a number of cells for the evaluation of this domain integral [1], and thus the dimensionality reduction merit of the method is lost. On the other hand, several other methods can be considered. For example, the double-reciprocity method has been proposed [2, 3]. However, the double-reciprocity method is not suitable for complicated inhomogeneous problems, because the domain must be divided into sub-domains in several cases.

Ochiai and Sekiya have proposed a method using the triple-reciprocity method for isotropic steady heat conduction [4]. Using this method, highly accurate solutions can be obtained solely by using a few terms of fundamental functions. In this method, the distribution is interpolated using the boundary integral equation. This paper demonstrates the two-dimensional triple-reciprocity BEM for the functionally gradient materials. The triple-reciprocity method is derived from the improved multiple-reciprocity method [5,6].

Theory

Steady heat conduction This study is concerned with the steady-state heat conduction problem for the functionally gradient materials. The governing equation can be expressed by [3]

$$\nabla\{\lambda^{S[1]}\nabla T(q)\}=0, \quad (1)$$

where $T(q)$ is the temperature at a point q , $\lambda^{S[1]}(q)$ the heat conductivity, and ∇ the gradient operator. The upper index S[1] indicates a distributed function. The governing differential equation is then expressed by

$$\nabla^2 T(q) = \frac{-1}{\lambda^{S[1]}(q)} \nabla \lambda^{S[1]}(q) \cdot \nabla T(q). \quad (2)$$

By BEM, the boundary integral equation for solving eq (2) is given by [1]

$$c(P)T(P) = \int_{\Gamma} \left[-\frac{\partial T_{[1]}^*(P,Q)}{\partial n} T(Q) + T_{[1]}^*(P,Q) \frac{\partial T(Q)}{\partial n} \right] d\Gamma + \int_{\Omega} \frac{1}{\lambda^{S[1]}(q)} \nabla \lambda^{S[1]}(q) \cdot \nabla T(q) T_{[1]}^*(P,q) d\Omega. \quad (3)$$

On the smooth boundary $c=0.5$ and in the domain $c=1$. The lower index [1] indicates the conventional

fundamental solution. The notations Γ and Ω represent the boundary and domain, respectively. The notations p and q become P and Q on the boundary. In a two-dimensional problem, the fundamental solution $T_{[1]}^*$ for steady heat conduction and its normal derivative are given by

$$T_{[1]}^*(P, Q) = \frac{1}{2\pi} \ln\left(\frac{1}{r}\right), \quad (4)$$

$$\frac{\partial T_{[1]}^*(P, Q)}{\partial n} = \frac{-1}{2\pi r} \frac{\partial r}{\partial n}, \quad (5)$$

where r is the distance between the observation point P and the loading point Q . When Eq (3) is used, the domain integral is required. Therefore, an interpolation method using boundary integral equations is introduced.

Interpolation In order to avoid the domain integral in eq (3), an interpolation method is introduced. The new function $W^{S[1]}(q)$ is defined as

$$W^{S[1]}(q) = \frac{1}{\lambda^{S[1]}(q)} \nabla \lambda^{S[1]}(q) \cdot \nabla T(q). \quad (6)$$

If the distribution of thermal conductivity $\lambda^{S[1]}$ is smooth, $\lambda^{S[1]}$ is interpolated as follows: [6,7]

$$\nabla^2 W^{S[1]} = -W^{S[2]}, \quad (7)$$

$$\nabla^2 W^{S[2]} = -W^{P[3]}. \quad (8)$$

From eqs (7) and (8), the following equation can be obtained.

$$\nabla^4 W^{S[1]} = W^{P[3]} \quad (9)$$

This equation is the same type as that for deformation $W^{S[1]}$ of a thin plate with unknown point load ($W^{P[3]}$). The value of point load ($W^{P[3]}$) is obtained inversely from the deformation $W^{S[1]}$ of the fictitious thin plate, as shown in Fig. 1(a). The $W^{S[2]}$ corresponds to the moment of the fictitious plate. The fictitious moment $W^{S[2]}$ on the boundary is assumed to be 0, the same as in the case for natural spline. This means that the fictitious thin plate is simply supported.

If the thermal conductivity $\lambda^{S[1]}$ is smooth as shown in Fig. 1(a), eqs (7) and (8) can be used. There are cases in which $W^{S[1]}$ is not smooth, because there is the term $\nabla \lambda^{S[1]}(q)$ in eq (6). When the thermal conductivity $\lambda^{S[1]}$ is not smooth as shown in Fig. 1(b) and (c), the next equations are used.

$$\nabla^2 W^{S[1]} = -\{W^{S[2]} + W^{L[2]} + W^{D[2]}\} \quad (10)$$

$$\nabla^2 W^{S[2]} = -W^{P[3]} \quad (11)$$

$W^{L[2]}$ in eq (10) corresponds to the line heat source in the heat conduction equation. This term $W^{L[2]}$ is used for expressing a ridge of the distribution as shown in Fig. 1(b). The height of the edge $W^{S[1]}$ is

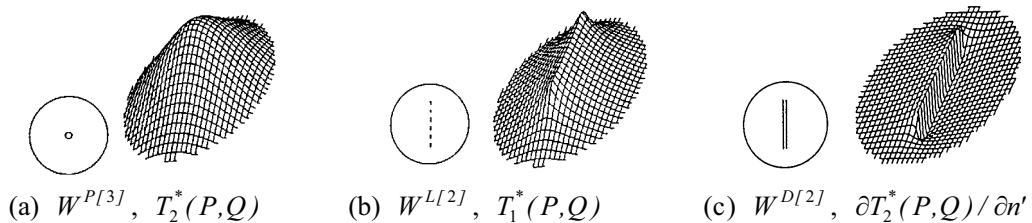


Fig.1 Various distributions of $\lambda^{S[1]}$ and $W^{S[1]}$

previously obtained, and the values of line heat sources $W^{L[2]}$ are obtained inversely. $W^{D[2]}$ in eq (10) is used for the discontinuous surface as shown in Fig. 1(c). $W^{D[2]}$ is the double-layer line potential, and it corresponds to a gap of the discontinuous surface. $W^{D[2]}$ is known value as a gap of the discontinuous surface. Using the above ideas, many kinds of distribution can be interpolated.

The polyharmonic function $T_{[f]}^*$ is defined by

$$\nabla^2 T_{[f+1]}^*(P, Q) = T_{[f]}^*(P, Q) \quad (12)$$

The polyharmonic function and its normal derivative are generally given by

$$T_{[f]}^*(P, Q) = \frac{r^{2(f-1)}}{2\pi[(2f-1)!!]^2} \left[\ln\left(\frac{1}{r}\right) + \text{sgn}(f-1) \sum_{e=1}^{f-1} \frac{1}{e} \right] \quad (13)$$

$$\frac{\partial T_{[f]}^*(P, Q)}{\partial n} = \frac{r^{2f-3}}{2\pi[(2f-2)!!]^2} \left[2(f-1) \ln\left(\frac{1}{r}\right) - 1 + 2(f-1) \sum_{e=1}^{f-1} \frac{1}{e} \right] \frac{\partial r}{\partial n} \quad (14)$$

where $\text{sgn}()$ is the sign function and $(2f-1)!! = (2f-1)(2f-3) \cdots 3 \cdot 1$.

On the other hand, the quantity of $W^{S[1]}$ is obtained by using Green's second identity two times, eqs (10), (11) and (12).

$$\begin{aligned} cW^{S[1]}(P) = & \sum_{f=1}^2 (-1)^f \int_{\Gamma} \left[\frac{\partial T_{[f]}^*(P, Q)}{\partial n} W^{S[f]}(Q) - T_{[f]}^*(P, Q) \frac{\partial W^{S[f]}(Q)}{\partial n} \right] d\Gamma - \sum_{m=1}^M T_{[2]}^*(P, q) W_{(m)}^{P[3]} \\ & + \int_{\Gamma^L} T_{[1]}^*(P, q^L) W^{L[2]}(q^L) d\Gamma^L + \int_{\Gamma^D} \frac{\partial T_{[1]}^*(P, q^D)}{\partial n'} W^{D[2]}(q^D) d\Gamma^D \quad (15) \end{aligned}$$

where the number of $W^{P[3]}$ is M , and n' is the unit normal to the line $W^{D[2]}$. Moreover, $W^{S[2]}$ in eq (11) is similarly given by

$$\begin{aligned} cW^{S[2]}(P) = & \int_{\Gamma} \left[-\frac{\partial T_{[1]}^*(P, Q)}{\partial n} W^{S[2]}(Q) \right. \\ & \left. - T_{[1]}^*(P, Q) \frac{\partial W^{S[2]}(Q)}{\partial n} \right] d\Gamma + \sum_{m=1}^M T_{[1]}^*(P, q) W_{(m)}^{P[3]}(q) \quad (16) \end{aligned}$$

In eqs (15) and (16), $W^{S[2]}(Q) = 0$ is assumed. In practice $W^{S[1]}$ is given, but $\partial W^{S[f]} / \partial n$ ($f=1,2$) and $W^{P[3]}$ and $W^{L[2]}$ in eq (15) and (16) are not given. These values must be calculated numerically.

In the same manner, the thermal conductivity $\lambda^{S[1]}$ is interpolated as follows:

$$\nabla^2 \lambda^{S[1]} = -\{\lambda^{P[2]} + \lambda^{L[2]} + \lambda^{D[2]}\} \quad (17)$$

$$\nabla^2 \lambda^{S[2]} = -\lambda^{P[3]} \quad (18)$$

From eqs (17) and (18), $\lambda^{S[1]}$ can be written as

$$\begin{aligned} c\lambda^{S[1]}(P) = & \sum_{f=1}^2 (-1)^f \int_{\Gamma} \left[\frac{\partial T_{[f]}^*(P, Q)}{\partial n} \lambda^{S[f]}(Q) \right. \\ & \left. - T_{[f]}^*(P, Q) \frac{\partial \lambda^{S[f]}(Q)}{\partial n} \right] d\Gamma - \sum_{m=1}^M T_{[2]}^*(P, q^P) \lambda_{(m)}^{P[3]}(q^P) \\ & + \int_{\Gamma^L} T_{[1]}^*(P, q^L) \lambda^{L[2]}(q^L) d\Gamma^L + \int_{\Gamma^D} \frac{\partial T_{[1]}^*(P, q^D)}{\partial n'} \lambda^{D[2]} d\Gamma^D \quad (19) \end{aligned}$$

Differentiating eq (19), we obtain

$$\begin{aligned} \frac{\partial \lambda^{S[1]}}{\partial x_i} = & \sum_{f=1}^2 (-1)^f \int_{\Gamma} \left[\frac{\partial^2 T_{[f]}^*(P, Q)}{\partial x_i \partial n} \lambda^{S[f]}(Q) \right. \\ & - \frac{\partial T_{[f]}^*(P, Q)}{\partial x_i} \frac{\partial \lambda^{S[f]}(Q)}{\partial n} \Big] d\Gamma - \sum_{m=1}^M \frac{\partial T_{[2]}^*}{\partial x_i} \lambda_{(m)}^{P[3]} \\ & + \int_{-L}^L \frac{\partial T_{[1]}^*(P, q^L)}{\partial x_i} \lambda^{L[2]} d\Gamma^L + \int_{-D}^D \frac{\partial^2 T_{[1]}^*(P, q^D)}{\partial x_i \partial n'} \lambda^{D[2]} d\Gamma^D, \end{aligned} \quad (20)$$

where

$$\frac{\partial T_{[f]}^*(P, Q)}{\partial x_i} = \frac{r^{2f-3}}{2\pi[(2f-2)!!]^2} \left[2(f-1) \ln\left(\frac{1}{r}\right) - 1 + 2(f-1) \sum_{e=1}^{f-1} \frac{1}{e} \right] r_{,i}, \quad (21)$$

$$\begin{aligned} \frac{\partial^2 T_{[f]}^*(P, Q)}{\partial x_i \partial n} = & \frac{r^{2f-4}}{2\pi[(2f-1)!!]^2} \left[\left\{ n_i + 2(f-2)r_i \frac{\partial r}{\partial n} \right\} \right. \\ & \left. \times \left\{ 2(f-1) \ln\left(\frac{1}{r}\right) - 1 + 2(f-1) \sum_{e=1}^{f-1} \frac{1}{e} \right\} - 2(f-1)r_i \frac{\partial r}{\partial n} \right]. \end{aligned} \quad (22)$$

Triple-reciprocity method Using eqs (10), (11) and Green's second identity, eq (3) becomes

$$\begin{aligned} cT = & \int_{\Gamma} \left[-\frac{\partial T_{[1]}^*(P, Q)}{\partial n} T(Q) + T_{[1]}^*(P, Q) \frac{\partial T(Q)}{\partial n} \right] d\Gamma + \sum_{f=1}^2 (-1)^f \int_{\Gamma} \left[-\frac{\partial T_{[f+1]}^*(P, Q)}{\partial n} W^{S[f]}(Q) \right. \\ & + T_{[f+1]}^*(P, Q) \frac{\partial W^{S[f]}(Q)}{\partial n} \Big] d\Gamma + \sum_{m=1}^M T_{[3]}^*(P, q^P) W_{(m)}^{P[3]}(q^P) \\ & - \int_{-L}^L T_{[2]}^*(P, q^L) W^{L[2]}(q^L) d\Gamma^L - \int_{-D}^D \frac{\partial T_{[2]}^*(P, q^D)}{\partial n'} W^{D[2]}(q^D) d\Gamma^D. \end{aligned} \quad (23)$$

$W^{S[1]}$ in eq (6) contains $\lambda^{S[1]}(q)$, $\nabla \lambda^{S[1]}(q)$ and $\nabla T^{S[1]}(q)$. The iteration process is necessary because there is unknown value caused by $\nabla T^{S[1]}(q)$. From eq (23), temperature gradient $\nabla T^{S[1]}(p)$ at an internal point is obtained by

$$\begin{aligned} \frac{\partial T(p)}{\partial x_i} = & \int_{\Gamma} \left[-\frac{\partial^2 T_{[1]}^*(p, Q)}{\partial x_i \partial n} T(Q) + \frac{\partial T_{[1]}^*(p, Q)}{\partial x_i} \frac{\partial T(Q)}{\partial n} \right] d\Gamma + \sum_{f=1}^2 (-1)^f \int_{\Gamma} \left[-\frac{\partial^2 T_{[f+1]}^*(p, Q)}{\partial x_i \partial n} W^{S[f]}(Q) \right. \\ & + \frac{\partial T_{[f+1]}^*(p, Q)}{\partial x_i} \frac{\partial W^{S[f]}(Q)}{\partial n} \Big] d\Gamma + \sum_{m=1}^M \frac{\partial T_{[3]}^*(p, q^P)}{\partial x_i} W_{(m)}^{P[3]}(q^P) \\ & - \int_{-L}^L \frac{\partial T_{[2]}^*(p, q^L)}{\partial x_i} W^{L[2]}(q^L) d\Gamma^L - \int_{-D}^D \frac{\partial^2 T_{[2]}^*(p, q^D)}{\partial x_i \partial n'} W^{D[2]}(q^D) d\Gamma^D. \end{aligned} \quad (24)$$

Using eq (24), the values $\nabla T^{S[1]}(q)$ at internal points are calculated, and $\nabla T^{S[1]}(P)$ on the boundary is obtained from eq (24). Then $W^{S[1]}(q)$ is obtained from eq (6), and $\nabla T^{S[1]}(q)$ is obtained from eq (24). This process is repeated several times for convergence. The internal random points are used for interpolation. Many internal points are necessary because the value of $W^{S[1]}$ is unknown. Especially, many internal points are necessary where the heat conduction coefficient changes heavily.

Numerical examples

In order to assure the accuracy of the present method, a heat conduction problem in a circular cylinder made of functionally gradient material is analyzed. The thermal conductivity $\lambda(r)$ in Fig. 2 is given by

$$\lambda(r) = \begin{cases} 125 - 250r & 0.2 \leq r \leq 0.3 \\ -100 + 500r & 0.3 \leq r \leq 0.4 \end{cases}, \quad (25)$$

Figure 2 shows the interpolated value of thermal conductivity. The solid line denotes the value given by eq (15). There is only one domain in Fig. 2. The internal line in Fig. 2 is used for interpolation in case of a distribution with a ridge line as shown in Fig. 1(b). The value of $W^{S[1]}$ in the case of eq (27) has a discontinuous distribution as shown in Fig. 1(c). Figure 4 shows the interpolated value of $W^{S[1]}$ by eq (15) with exact values. Figure 5 shows the temperature distribution. The solid line in Fig. 5 denotes the exact value.

Next, a heat conduction problem in the same square region of side $L=1\text{m}$ as shown in Fig.6 is analyzed with two-dimensional distribution of thermal conductivity. The thermal conductivity is given by

$$\lambda(x, y) = 1 + 2 \sin\left(\frac{\pi x}{L}\right) \sin x\left(\frac{\pi y}{L}\right). \tag{26}$$

Figure 7 shows the interpolated value of thermal conductivity at $y=0.5, 0.3$ and 0.1 m with values given by Eq.(26). Figure 8 shows temperature distribution with the solution obtained by FEM. A total 100 PLANE55 elements are used in ANSYS (FEM) to model the domain.

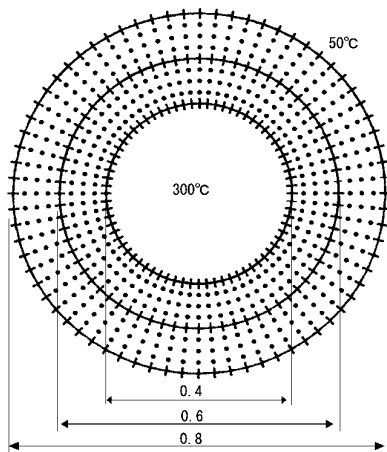


Fig.2 Circular region with nonsmooth distribution

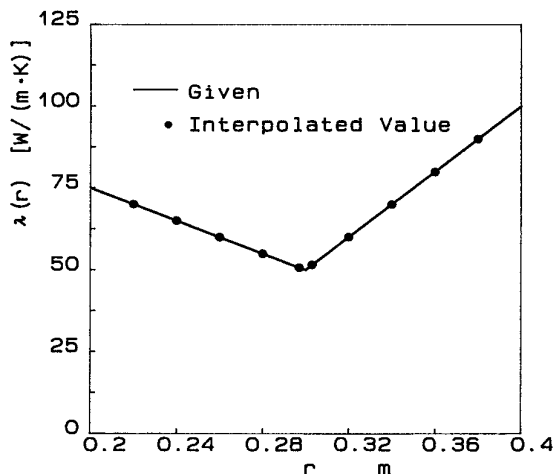


Fig.3 Interpolation of thermal conductivity λ

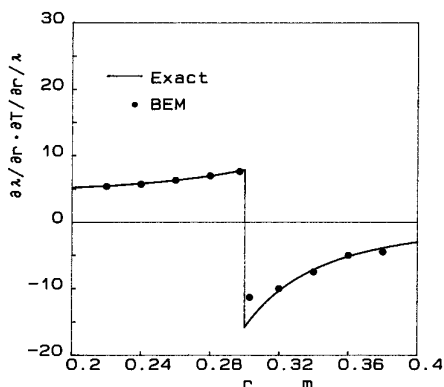


Fig.4 Distribution of $W^{S[1]}$

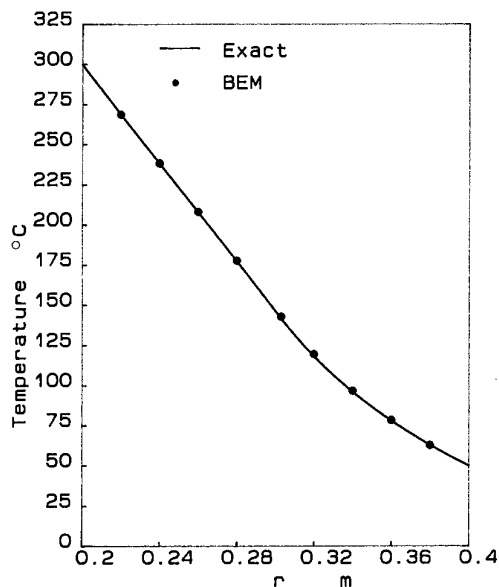


Fig.5 Temperature distribution

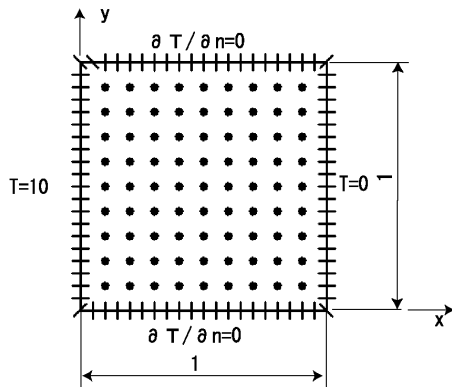


Fig.6 Boundary elements and internal points

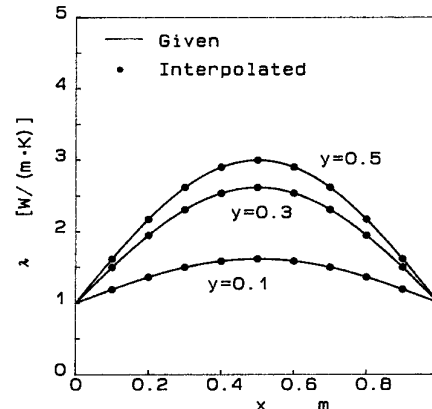


Fig.7 Interpolation of thermal conductivity $\lambda(x,y)$

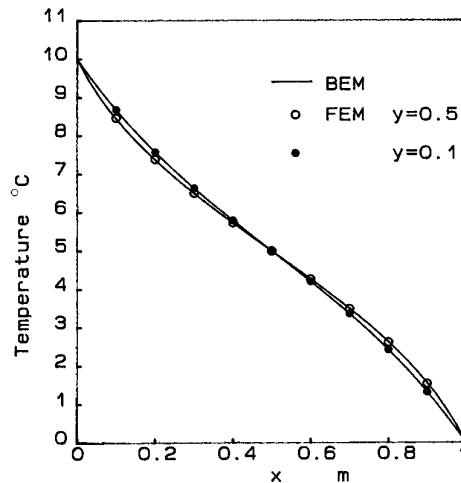


Fig.8 Temperature distribution of functionally gradient materials

Summery

The steady heat conduction analysis of a functionally gradient material was solved without internal cells by the triple-reciprocity BEM. The distribution is interpolated using the polyharmonic function and boundary integral equations. It was shown that it is possible to express the complicated distribution with a ridge line and discontinuous distribution. Even for complicated distribution, it is not necessary to divide the domain. From numerical computations of some examples, it is revealed that the proposed method is applicable to the steady-state heat conduction problem of FGM.

References:

[1] Brebbia, C. A., Tells, J. C. F, and Wrobel, L. C., *Boundary Element Techniques-Theory and Applications in Engineering*, pp.47-107, Berlin, Springer-Verlag (1984).

[2] Partridge, P. W., Brebbia, C.A. and Wrobel, L. C. , *The Dual Reciprocity Boundary Element Method*, Computational Mechanics Publications, pp.223-253, (1992).

[3] Tanaka, M., Matsumoto, T. and Suda, Y., *A Dual Reciprocity Boundary Element Method Applied to the Steady-State Conduction Problem of Functionally Gradient Material*, *Advances in Boundary Element Techniques II* , Hoggar, pp.173-180, (2001).

[4] Ochiai, Y. and Sekiya, T., *Steady Heat Conduction Analysis by Improved Multiple-Reciprocity Boundary Element Method*, *Engineering Analysis with Boundary Elements*, Vol.18, pp.111-117, (1996).

[5] Ochiai, Y. and Kobayashi, T., *Initial Strain Formulation without Internal Cells for Elastoplastic Analysis by Triple-reciprocity BEM*, *Int. J. for Numerical Methods in Engineering*, Vol.50, pp.1877-1892, (2001).

[6] Ochiai, Y., *Multidimensional Numerical Integration for Meshless BEM*, *Engineering Analysis with Boundary Elements*, Vol.27, No.3, pp.241-249, (2003).

Multipole BEM for the analysis of Stokes flow

A. Frangi¹, A. di Gioia²

¹ Dept. of Structural Engng., Politecnico di Milano, Milan, Italy
(attilio.frangi@polimi.it)

² Dept. of Structural and Mechanical Engng., University of Trento, Trento, Italy
(arturo.digioia@ing.unitn.it)

Keywords: BEM, Multipole, Stokes flow, MEMS

Abstract. In the context of an industry-oriented multi-physics code a module for the analysis of Stokes flow around complex micro structures is developed employing first kind integral equations (single layer kernels) and multipole accelerators, with specific attention to preconditioners for the iterative linear solvers.

Introduction and formulation

Micro-Electro-Mechanical-Systems (MEMS) are complex micro-structures employed as sensors or actuators in resonators, accelerometers, micro-mirrors, micro-pumps etc. In this contribution we focus on silicon or metallic MEMS displaying movable and fixed parts which often can be simulated as rigid structures with concentrated elasticity (e.g. linear or rotational springs), especially at a first stage of the design and analysis steps.

A correct analysis of such MEMS generally requires a multi-physics code coupling the rigid body dynamics of the movable part with the electrostatic field and the viscous flow of the gas around the micro-structure.

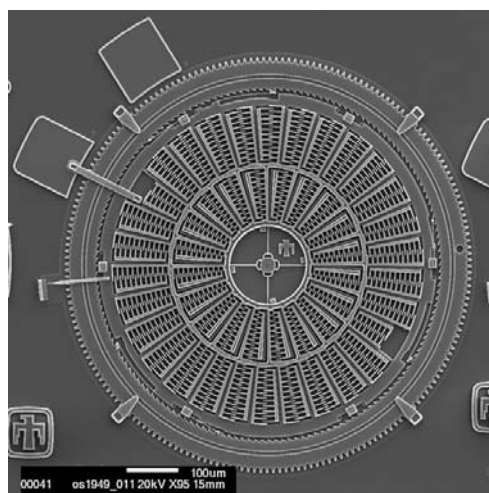


Figure 1: Example of MEMS structure: torsional accelerometer

Due to the problem micro-scale the Reynolds numbers associated to the flow are generally low enough to allow for the application of the steady state incompressible Stokes model. Moreover, if such an approximation is deemed acceptable, a pure BEM code can be applied with the considerable benefit that large relative displacements and rotations among the different modules can be easily accounted for with minimal remeshing.

The main drawback is that when the problem size grows in 3D, the application of iterative solution procedures and accelerators (or *compressors*) become mandatory since BEM matrices are full. The standard multipole techniques implemented herein (see the citations in [1,3]) allow to utilize iterative solvers in the sense that they reduce the operation count per iteration to approximately $O(N \log N)$ (to be compared with the standard $O(N^2)$ for classical approaches, where N is the problem dimension).

Unfortunately, when iterative solvers are employed, spectral properties of the matrix stemming from problem discretisation and preconditioning become major issues and will be discussed in the sequel.

Various approaches have been adopted in the literature for the analysis of Stokes flow via integral equations [6,7] and some of these methodologies have been recently compared in [3]. However most of the contributions concern 2D problems or simple 3D geometries (e.g. interacting spheres) while the main issue of MEMS is complexity; moreover few concern applications of accelerator approaches (see however the 2D cases analysed in [1,2,4] and the wavelet condensation put forward in [9]). The approaches available fall essentially in two main categories: direct and indirect methodologies.

The most straightforward direct approach employs the Somigliana identity for incompressible elasticity, which specified to the problem at hand write:

$$u_i(\underline{y}) = \int_S G_{ij}(\underline{y}, \underline{x}) t_j(\underline{x}) dS \quad (1)$$

$$G_{ij}(\underline{y}, \underline{x}) = \frac{1}{8\pi r} (\delta_{ij} + r_i r_j)$$

Surface S is the outer surface of the rigid solid structures, vector \underline{u} denotes given fluid velocity at the collocation points \underline{y} on S , \underline{t} are tractions on S , and \underline{r} is the distance vector between the source and field points \underline{y} and \underline{x} .

Equation (1), collocated at point on the boundary, is used to solve the so called *resistance* problem in which the velocity of the moving rigid body is given and the \underline{t} field is computed. The global damping forces and couples acting on the structures are computed during a post-processing phase from \underline{t} .

Two major remarks arise: i) eq(1) has a non trivial kernel containing $\underline{n}(\underline{x})$, where $\underline{n}(\underline{x})$ is the outward normal to any closed structure analysed; ii) eq(1) is a first kind integral equation leading to a dense linear system whose spectral condition number strongly depends on the discretisation used. Remedies to point i) are well known and basically consist in filtering the kernel base out of the solution. Remedies to point ii) represent the key to a successful implementation for large scale problems and are still an open issue.

The problem mentioned in point ii) has essentially motivated in the past the choice of *indirect* approaches, among which a major role is played by the Completed Double Layer Integral Equation (CDL BIE) [1,3,6,7] where double layer kernels are employed instead of the weakly singular single layer one in eq(1). In [3] it is shown that the condition number of the linear system is considerably better than for the direct single layer approach. However, the comparison is always conducted on particularly simple structures. On the contrary, when applied to the complex structures of MEMS in this investigation, the CDL-BIE proved to behave very poorly in

comparison to the direct approach and has been hence abandoned in favor of eq(1) with suitable preconditioners.

A commonly adopted approach with multipole consists in utilizing the octree structure also in order to produce a preconditioner. Indeed the structure is partitioned in a series of non overlapping cubes of different sizes containing at most Q elements, where Q is a fixed parameter (here $Q = 200$). For each of these *leaves* the full matrix of the elements within that leaf is constructed. The leaves preconditioner (LP) consists in inverting the block diagonal matrix obtained by assembling all the sub-matrices of the leaves. This approach works properly in most cases, but not for complex comb-fingers structures like those presented in Figure 1. In this latter case a different approach is utilized, based on physical remarks. For process reasons MEMS structures consist of several repetitive blocks, called units. In Figure 1 each finger represents a unit, for instance. It has been observed that the code performance is considerably enhanced if the diagonal blocks of the preconditioner are built considering the elements in each unit instead of utilizing the leaves (unit preconditioner, LP).

Preliminary results

The two examples presented in this section have been analysed using a piecewise constant interpolation for tractions. Equation (1) is collocated at the centre of each element. The system is solved using a GMRES routine. The final goal of the analysis is the evaluation of the viscous drag on the sphere. It has been observed experimentally that the error in the global force is comparable with the residual computed by the GMRES routine (residual divided by the rhs norm). The stopping criterion for the GMRES solver is hence always relatively mild (10^{-4}).

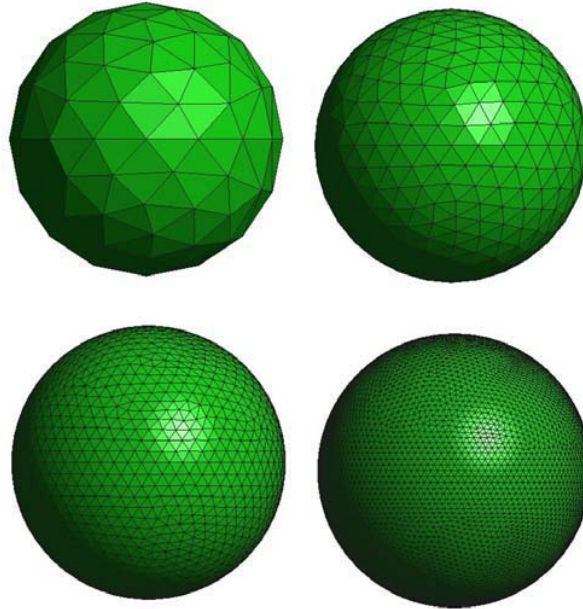


Figure 2: Meshes employed for the analysis of the sphere

Translating sphere. The classical benchmark of a translating sphere is first addressed to test accuracy of the proposed methodology. The sphere is moving with constant velocity V along a fixed direction. The global force acting on the sphere is $F=6\pi\mu aV$, with μ air viscosity, a sphere radius. This example has been solved using LP.

Mesh	Num. elem.	Num. unknowns	Force $F/(\mu aV)$	Iterations
1	208	824	184.103	10
2	800	2400	187.23	11
3	3144	9432	188.04	12
4	12654	47962	188.95	16
exact			188.495	

Table 1: Results for the translating sphere

Table 1 collects some data and results concerning the analyses. It should be remarked that the number of iteration required to reach convergence (relative residual $\varepsilon = 10^{-4}$) is little sensitive to mesh refinement. Unfortunately this proves to be a coincidence. It is worth remarking that the finest mesh converges in about 200 seconds on a DELL Windows desktop with a Pentium 4 2.6GHz processor.

Comb-finger structure. As a second example a comb-finger structure (Figure 3) is analysed. The structure is made a fixed part (the stator) and a moving part (the rotor). The movement occurs in a direction orthogonal to the fingers opposing surfaces.

Mesh	Num. elem.	Num. unknowns	Iterations (leaves)	Iteration (units)
1	784	2353	104	104
2	5292	15876	188	110
3	14868	44604	>300	131

Table 2: Results for the comb-finger structure

This turns out to be a formidable benchmark for the adopted formulation. Both LP and UP have been utilized and the performances are collected in Table 2 in terms of number of iterations. In this case each finger is considered as a unit. The preconditioning phase is performed by solving each sub-problem defined on a unit by direct approaches.

As expected, UP turns out to be much less sensitive to mesh refinement than LP.

Conclusions

The implementation of a BIE approach for the analysis of drag forces on 3D micro-structures (MEMS) has been developed employing fast multipole accelerators. Encouraging results have been obtained, but further research is required.

Preconditioners represent the major issue in iterative analyses. A general purpose very elegant but involved pre-conditioner for first kind integral equations has been proposed in [8]. Its application to the problem at hand is not straightforward and is still under investigation. Alternatively, the “unit preconditioner” adopted herein has proved to be effective. The difficulty represented by the automatic definition of the sub-units seems to be of minor importance in this context where repetitivity of structures provides an easy to implement criterion.

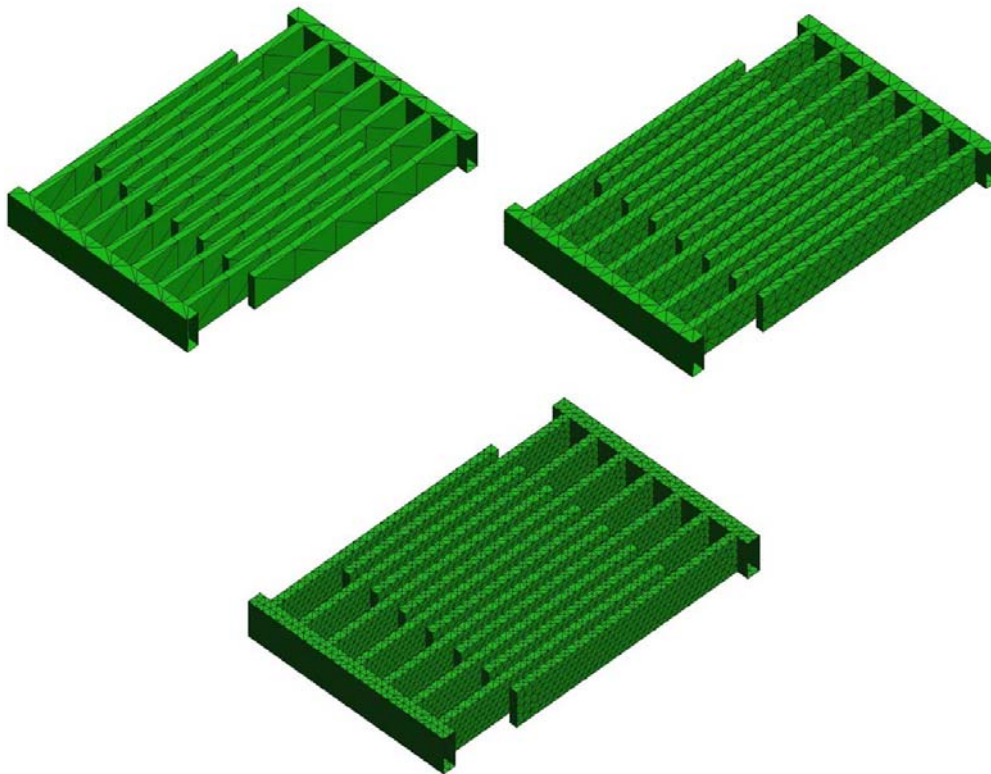


Figure 3: Meshes employed for the analysis of the comb-finger structures

Acknowledgments

Financial support from “Design for Micro & Nano Manufacture (PATENT-DfMM)” Network of Excellence is gratefully acknowledged

References

- [1] G. Biros, L. Ying, D. Zorin, A fast solver for the Stokes equations with distributed forces in complex geometries, *Journal of Computational Physics*, **193**, 317-348 (2003)
- [2] J.E. Gomez and H. Power, A multipole direct and indirect BEM for 2D cavity flow at low Reynolds number, *Engineering Analysis with Boundary Elements*, **19**, 17-31 (1997).
- [3] M.S. Ingber and A.A. Mammoli, A comparison of integral formulations for the analysis of low Reynolds number flows, *Engineering Analysis with Boundary Elements*, **23**, 307-315 (1999).
- [4] A.A. Mammoli and M.S. Ingber, Stokes flow around cylinders in a bounded two-dimensional domain using multipole-accelerated boundary element methods, *International Journal for Numerical Methods in Engineering*, **44**, 897-917 (1999)

- [5] S. Nasser, N. Phan-Thien, X.J. Fan, Lubrification approximation in completed double layer boundary element method, *Computational Mechanics*, **26**, 388-397 (2000)
- [6] H. Power and L. Wrobel, *Boundary Integral Methods in Fluid Mechanics*, Computational Mechanics Publications, Southampton (1995)
- [7] C. Pozrikidis, *Boundary Integral and Singularity Methods for Linearized Viscous flow*, Cambridge University Press, Cambridge (1992)
- [8] O. Steinbach and W.L. Wendland, The construction of some efficient preconditioners in the boundary element method, *Advances in Computational Mathematics*, **9**, 191,216 (1998)
- [9] J. Tausch, Sparse BEM for potential theory and Stokes flow using variable order wavelets, *Computational Mechanics*, **32**, 312-318 (2003)

BEM for Thermal Design of Hollow Bricks

Božidar Šarler, Robert Vertnik and Igor Bric

Laboratory for Multiphase Processes, Nova Gorica Polytechnic, Slovenia.

email: bozidar.sarler@p-ng.si

Keywords: boundary element method, hollow bricks, thermal design.

Abstract. The Boundary Element Method (BEM) is applied to steady heat conduction problems with temperature dependent thermal conductivity, and all types of technically relevant boundary conditions. The method is structured by using discontinuous linear boundary elements and Laplace fundamental solution. The non-linear material property is overcome by using the Kirchhoff's transform. The developed method is particularly advantageous in geometrically complex situations. Respectively, several two dimensional thermal design calculations of hollow-bricks with realistic sophisticated geometry and realistic material properties are performed.

Introduction

The brick walls are known to possess classic beauty, strength, lasting value, energy efficiency, and low maintenance. However, the efficient use of energy resources poses ever new challenges to the design of bricks. In this paper, the BEM is used for solving the heat conduction problem, associated with the temperature fields in complicately shaped hollow bricks. The BEM is a numerical technique [1,2] that falls in the class of methods generally called boundary methods. The other well known representative of these methods is the Method of Fundamental Solutions (MFS) [3]. Both methods are best applicable in situations where a fundamental solution to the partial differential equation in question is known. In such cases, the dimensionality of the discretization is reduced. BEM for example requires polygonisation of the boundary surfaces in general 3D cases, and boundary curves in general 2D cases. The method requires solution of the complicated regular, weakly singular, strongly singular, and hypersingular integrals over boundary segments which is usually a cumbersome and non-trivial task. The MFS has certain advantages over BEM, that are mostly visible in the fact that pointisation of the boundary is needed only, that completely avoids any integral evaluations, and makes no principal difference in coding between the 2D and the 3D cases. The principal drawback of MFS represents the fact that an artificial boundary needs to be generated around the physical boundary for positioning the fundamental solution poles. The present group first applied the MFS to the problem of thermal design of hollow bricks [3]. Recently, the solver has been exchanged with the classical BEM solver, described in this work. The reasons for the change are elaborated in the conclusions.

Governing equations

This paper deals with the steady heat conduction problem in material with the temperature T dependent isotropic thermal conductivity k

$$k = k(T) \quad (1)$$

confined to domain Ω with the boundary Γ . The problem physics is described as

$$\bar{\nabla} \cdot (k \bar{\nabla} T) = 0 \quad (2)$$

The boundary Γ is divided into connected or disjoint parts Γ^D, Γ^N and Γ^R :
 $\Gamma = \Gamma^D \cup \Gamma^N \cup \Gamma^R$ with Dirichlet, Neumann and Robin type boundary conditions, respectively. These boundary conditions are at the boundary point \vec{p} with normal \vec{n}_r defined through known functions T^D, T^N, T^R and T_{ref}^R

$$T = T^D; \vec{p} \in \Gamma^D \quad (3)$$

$$\frac{\partial}{\partial n_r} T = -\frac{T^N}{k}; \vec{p} \in \Gamma^N \quad (4)$$

$$\frac{\partial}{\partial n_r} T = -\frac{T^R}{k}(T - T_{ref}^R); \vec{p} \in \Gamma^R \quad (5)$$

The equation (2) and boundary conditions (3,4,5) are transformed into equivalent form by Kirchhoff's transform

$$T(T) = \int_{T_0}^T \frac{k(\theta)}{k_0} d\theta \quad (6)$$

where T_0 represents the reference temperature, and k_0 the reference thermal conductivity. The inverse Kirchhoff's transform $T(T)$ and the derivative $dT(T)/dT$ are also assumed to be known. The Kirchhoff's transformed equation (2) with the adjacent boundary conditions (3,4,5) reads

$$k_0 \bar{\nabla}^2 T = 0 \quad (7)$$

$$T = T(T^D); \vec{p} \in \Gamma^D \quad (8)$$

$$\frac{\partial}{\partial n_r} T = -\frac{T^N}{k_0}; \vec{p} \in \Gamma^N \quad (9)$$

The Robin boundary conditions have to be treated in an iterative way, due to the nonlinearity of the function $T(T)$ that appears in a general case. For this purpose, the temperature variable is Taylor expanded around Kirchhoff variable \bar{T} , known from the previous iteration

$$\frac{\partial}{\partial n_r} T = -\frac{T^R}{k_0} \left[T(\bar{T}) + \frac{dT}{dT}(\bar{T})(T - \bar{T}) - T_{ref}^R \right]; \bar{p} \in \Gamma^R \quad (10)$$

This enables the Kirchhoff variable to be explicitly present in the formulation of the Robin boundary conditions – similarly like temperature in the non-transformed original problem.

Solution procedure and numerical examples

The transformed equation is weighted with the fundamental solution of the Laplace equation

$$T^* = \frac{1}{2\pi} \log \frac{r_0}{r}; r^2 = \vec{r} \cdot \vec{r}, r = r_x i_x + r_y i_y, r_x = p_x - s_x, r_y = p_y - s_y \quad (11)$$

over the domain Ω , where r_0 represents the reference radius, p_x, p_y , denote Cartesian coordinates (base vectors \vec{i}_x, \vec{i}_y) of point \vec{p} , and s_x, s_y Cartesian coordinates of fundamental solution source point \vec{s} , respectively. After application of the Green's second identity, the following standard integral form is obtained

$$\int_{\Gamma} \frac{\partial}{\partial n_r} T(\vec{p}) T^*(\vec{p}, \vec{s}) d\Gamma - \int_{\Gamma} T(\vec{p}) \frac{\partial}{\partial n_r} T^*(\vec{p}, \vec{s}) d\Gamma - c_s^* T(\vec{s}) = 0 \quad (12)$$

Boundary geometry is approximated by N_r straight line segments, and spatial variation of fields on each of the boundary segments is represented by constant interpolation functions. The discretized form of (12) reads

$$\sum_{i=1}^{N_r} \frac{\partial}{\partial n_r} T_i \int_{\Gamma_i} T^*(\vec{p}, \vec{s}) d\Gamma - \sum_{i=1}^{N_r} T_i \int_{\Gamma_i} \frac{\partial}{\partial n_r} T^*(\vec{p}, \vec{s}) d\Gamma - c_s^* T(\vec{s}) = 0 \quad (13)$$

The unknown Kirchhoff variable in Neumann and Robin boundary points and unknown heat fluxes in Dirichlet boundary points are calculated in a classical collocation way. The adjacent $N_r \times N_r$ matrix is solved by the IMSL package of Compaq Visual Fortran with the routines LUDCMP and LUBKSB for LU decomposition and back-substitution. All involved integrals are solved in a closed form [5]. The typical discretization of bricks shown in Figures 1-4 is around 6000 nodes. All bricks are calculated with the temperature $-20^\circ C$ on the left boundary, $+20^\circ C$ on the right boundary, and with the clay thermal conductivity $0.6 W/(mK)$.

The BEM solver has been embedded in a user friendly input-output interface coded in Borland Delphi. The graphical output displays also several technological parameters such as brick's thermal resistivity and conductance.

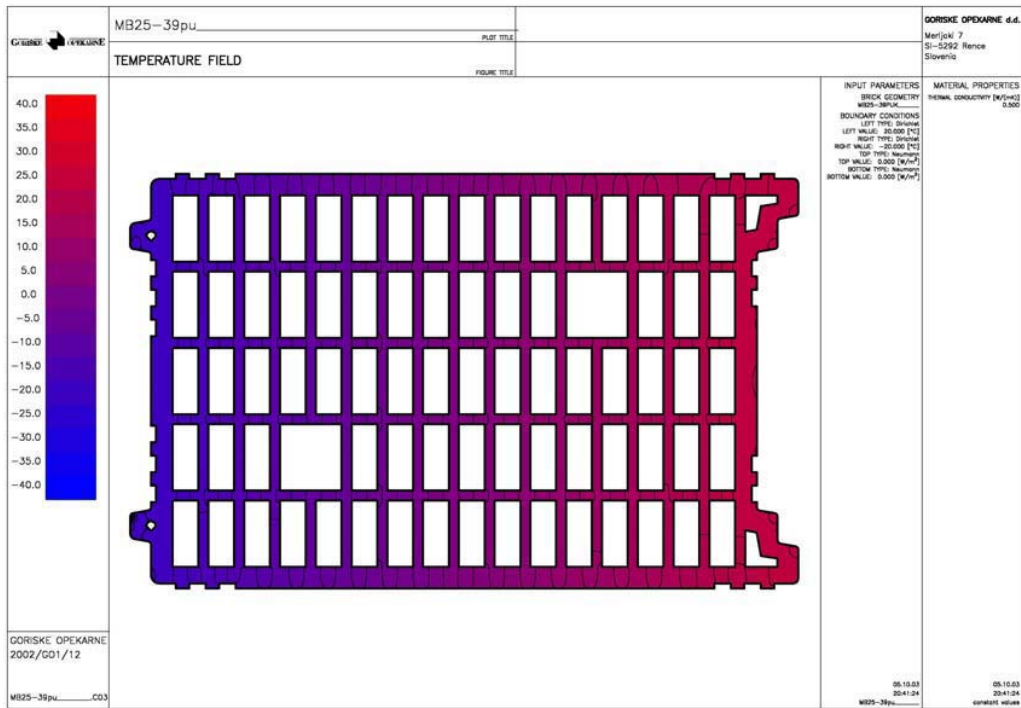


Fig. 1: Temperature field of the brick MB25.

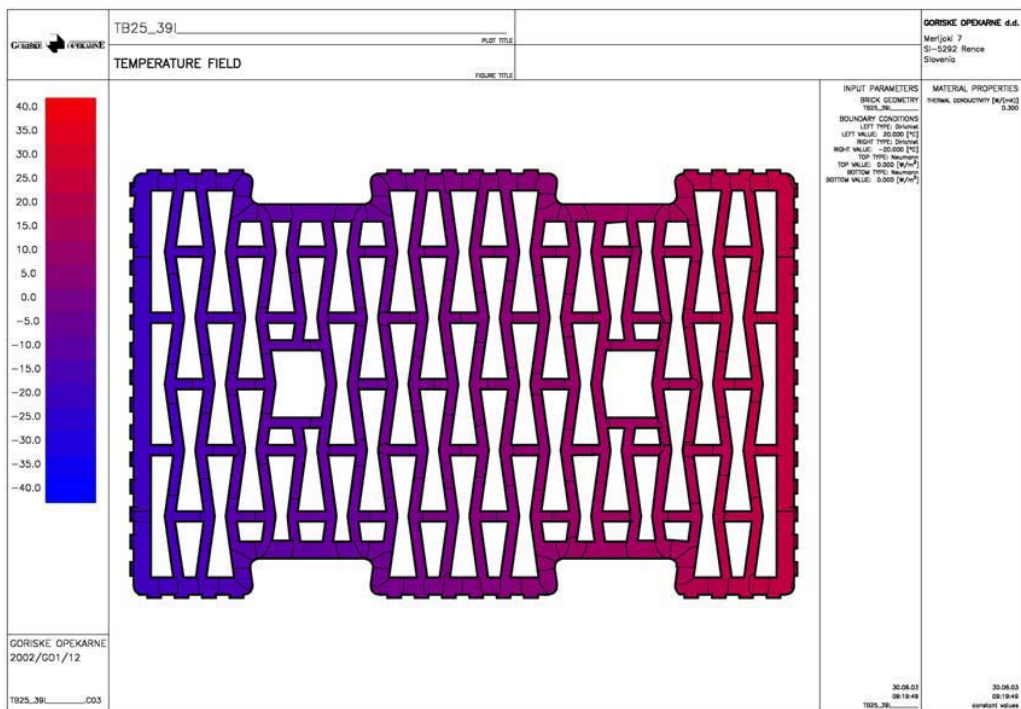


Fig. 2: Temperature field of the brick TB25.

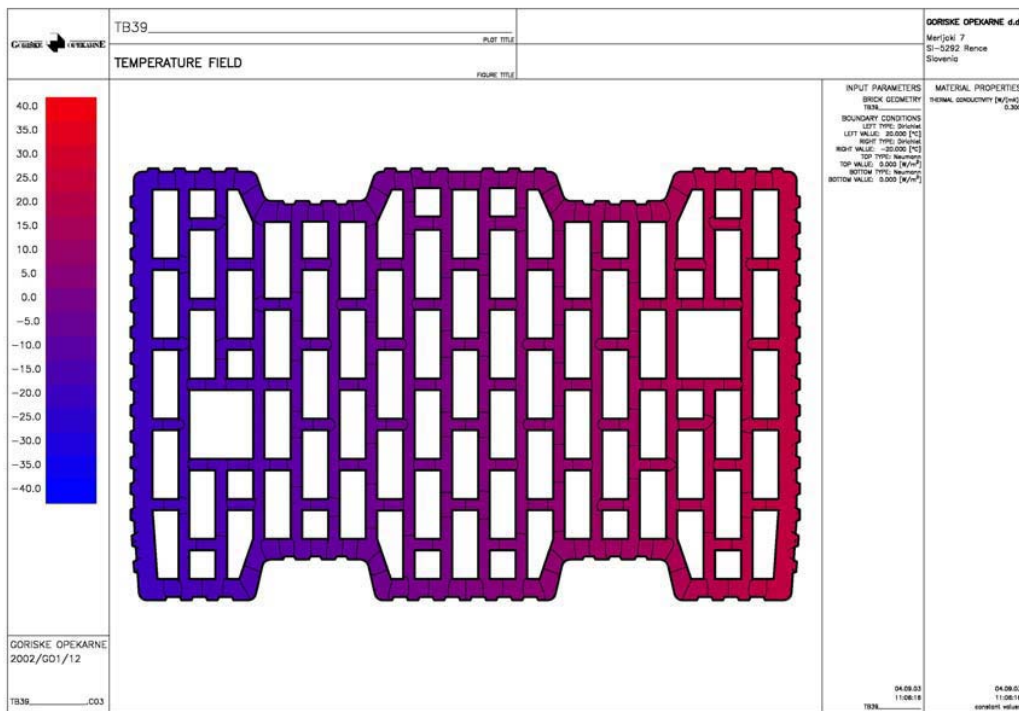


Fig. 3: Temperature field of the brick TB39.

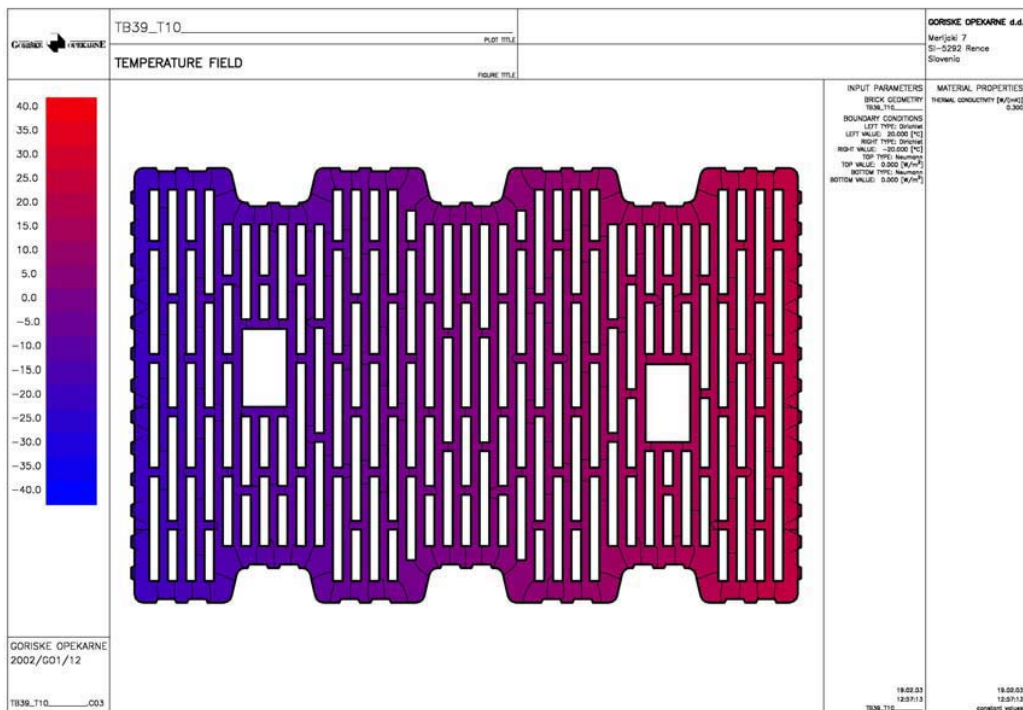


Fig. 4: Temperature field of the brick TB39-T10.

Conclusions

This study shows an engineering application of the BEM in one of the fields for which it appears to be best suited. BEM is from the numerical implementation point of view a little more complicated than the MFS because of the involved discretisation of the boundary and subsequent integration. However, the expense of boundary discretisation and calculation of the boundary integrals more than out-weighs the complications with the artificial boundary (position not known a-priori), encountered in our similar study with MFS. Our research is now focusing on upgrading of the numerical model with the natural convection in the air filled brick holes. One of the possibilities is to use the Radial Basis Function Collocation method [6]. The present thermal model will transfer Dirichlet boundary conditions for the natural convection calculations in each of the holes, and the results of the natural convection calculation will transfer back the new Neumann boundary conditions (heat fluxes) to the heat conduction model, until convergence. The complicated heat conduction-natural convection model will be in the future coupled also with the stress-strain calculations that intends to be performed on the mesh-free basis. The final aim of the represented computational model is in the assessment of the possible improvements of the brick thermal resistivity, mechanical strength, and brick weight at the same time, as a function of the number of holes, their dimensions, and manufacturing constraints. For this purpose, the methodology described in [7] will be used.

Acknowledgement

The authors wish to express their gratitude to Brickworks Goriške opekarne www.go-opekarne.si for funding and permission to publish this work.

References

- [1] L.C. Wrobel, *The Boundary Element Method, Vol.1: Applications in Thermo-Fluids and Acoustics*, Wiley (2002).
- [2] M.H. Aliabadi, *The Boundary Element Method, Vol.2: Applications in Solids and Structures*, Wiley (2002).
- [3] G. Fairweather, A. Karagheorghis, The method of fundamental solutions for elliptic boundary value problems, *Advances in computational mathematics*, **9** (1998) 69-95.
- [4] B.Šarler, R.Vertnik, M.Savić, A meshless approach to hollow-brick temperature field, S. Atluri, D.W. Pepper (eds.) *Advances in computational engineering & sciences, ICES'02*, Tech.Science Press, (2002).
- [5] Z. Rek and B. Šarler, Analytical integration of elliptic 2D fundamental solution and its derivatives for straight-line elements with constant interpolation. *Engineering analysis with boundary elements* **23**, 515-525 (1999).
- [6] B. Šarler, J. Perko and C.S. Chen, Radial basis function collocation method solution of natural convection in porous media. *International journal of numerical methods for heat & fluid flow* **14**, 187-212 (2004).
- [7] F. Hediger, Automatic process optimization in materials technology, EU-COST-526, www.access.rwth-aachen.de/apomat/.

BEM solution for continuous casting of alloys

R. Cholewa¹, A. J. Nowak¹, L.C. Wrobel²

¹Institute of Thermal Technology, Silesian University of Technology, 44-101 Gliwice, Konarskiego 22, Poland, nowak@itc.ise.polsl.gliwice.pl

²Brunel University, Uxbridge, Middlesex, UB8 3PH, United Kingdom

Keywords: BEM solution of diffusion-convection problem, continuous casting of alloys, nonlinear materials

Abstract This paper presents a two-dimensional heat transfer analysis of the continuous casting process of materials which solidifies in the range of temperatures (alloys). The temperature field is found by BEM using dual reciprocity and Kirchhoff's transformation in case of nonlinear material properties. The position of the mushy zone is searched iteratively by the front tracking technique. Numerical examples are included and discussed.

Introduction

In the continuous casting process liquid metal is poured into the mould whose walls are cooled by the flowing water. Consequently, the whole system disperses the heat and the liquid phase solidifies. For a pure metal solidification takes place at a constant temperature, while for alloys liquid and solid phases are separated by the mushy zone in which both phases appear at the same time. The side surface of the obtained ingot is still very intensively cooled by water flowing out of the mould and being sprayed over the surface. The cooled ingot is pulled out by withdrawal rolls at a constant rate.

In general, there are two main approaches to the solution of the solidification problem: the front tracking method and the fixed domain method. Until now the heat transfer analysis of the continuous casting process of alloys has been primarily dealt with the fixed domain method [7]. In the front tracking method analysis was only carried out making unrealistic assumption that metal solidifies at a constant temperature [4].

On the other hand, the front tracking method was successfully used for pure metals. For example, in the author's earlier works [1]-[3] it was shown how to effectively carry out analysis using Bezier splines and BEM. In those papers the solution procedures started from the assumption of the initial position of the phase change front approximated by Bezier splines. Then the heat transfer problem was formulated and solved by BEM in two existing subdomains forcing continuity in the temperature field. Since the temperature obtained along the initial location of the front is different from melting point, the position of the phase change front in the next iteration was changed using the front tracking algorithm. Because the application of the Bezier splines reduces the number of variables describing location of the front it was possible to search for the position of the phase change front by minimisation of the objective function.

The main objective of this work is to adapt the algorithm described above to analysis of materials which solidifies in the range of temperatures. Following other authors the three subdomains: the liquid phase, the solid phase and the mushy zone are introduced. It was also assumed that liquid fraction changes its value only with temperature and the solute distribution within the cast is uniform.

The solution procedure starts from the assumption of the location of both interfaces, *i.e.* solidus and liquidus. Then heat transfer equation in each phase is solved by BEM using Kirchhoff's transformation and dual reciprocity technique with the option capable of dealing with nonlinear material properties. In the mushy zone realisation of the latent heat is taken into consideration by means of the apparent heat capacity. In the next iteration the positions of the solidus and liquidus are corrected applying the front tracking algorithm. Similarly to algorithm developed for pure metal this equivalent

to minimisation of the objective function. It is also proposed to approximate both solidus and liquidus by Bezier splines.

Representative numerical examples showing the main features of the algorithm, as convergence of the iteration process and accuracy are included.

Mathematical model and applied algorithms

The 2-D geometrical domain which refers to the continuous casting processes and applied boundary conditions along the side of the ingot are schematically shown in Fig. 1.

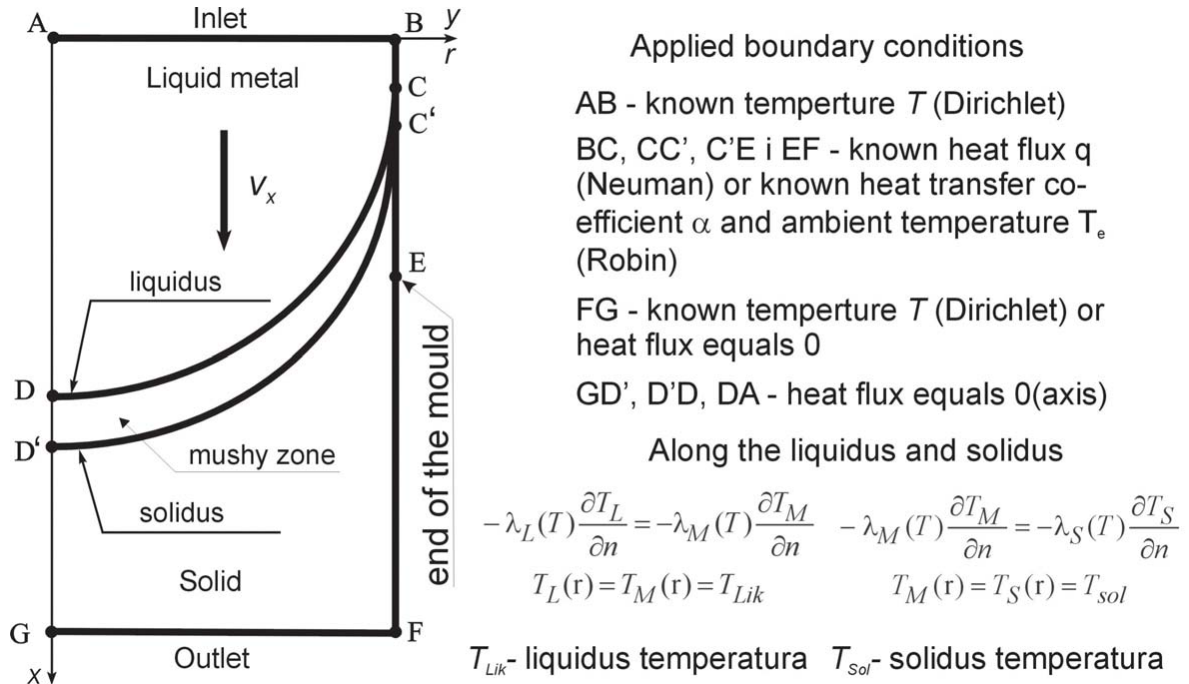


Figure 1: The continuous casting system.

In the previous author's works it was proved that neglecting natural convection in the liquid phase does not influence on the obtained result significantly. Hence the governing equation that describes the steady-state diffusion-convection heat transfer in all three subdomains, can be written in the form:

$$\nabla (\lambda(T) \nabla T) = \rho(T) c_z(T) v_x \frac{\partial T}{\partial x} \tag{1}$$

In the mushy zone $c_z(T)$ represents substitute heat capacity, while for the liquid and solid phase $c_z(T)$ is the heat capacity of the liquid and solid respectively. The substitute heat capacity in the mushy zone can be calculated from equation:

$$c_z(T) = c_{LS}(T) - L \frac{\partial S(T)}{\partial T} \tag{2}$$

where L is the latent heat and S stands for the solid phase fraction

In the case of constant material properties the standard BEM procedure can be used and the solution of the boundary problem is expressed by the following system of linear equations:

$$H T = G Q \tag{3}$$

where the vectors \mathbf{T} and \mathbf{Q} contain nodal temperatures and heat fluxes, respectively. \mathbf{H} and \mathbf{G} stand for the BEM influence matrices, the coefficients of which result from the integration of the fundamental solution of the diffusion-convection equation, and its normal derivative, over each boundary element. Expressions for these coefficients can be written (see [8]) as follows:

$$H_{kj} = \lambda c_k \delta_{kj} + \sum_e \int_{S_e} N_j^e \left(q^* - \frac{\lambda}{a} u^* v_x n_x \right) dS \quad (4)$$

$$G_{kj} = \sum_e \int_{S_e} N_j^e u^* dS \quad (5)$$

where δ_{kj} represents the Kronecker symbol and N_j^e stands for the interpolation function associated with the temperature T_j and/or heat flux q_j within the considered element e . Summation is made over all elements sharing the node j , and the constant c_k depends on the angle the boundary makes at the collocation point. Details of how to find the fundamental solution u^* and its normal derivative q^* can be found elsewhere, e.g. in [8].

For the temperature dependent material properties Kirchoff's transformation is used and the following equation is obtained:

$$\lambda_0 \nabla^2 \varphi = \rho c(T) v_x \frac{\partial T}{\partial x} \quad (6)$$

where constant φ_0 , and λ_0 are the values of Kirchoff's transform and thermal conductivity for reference temperature T_0 . Since the fundamental solution for equation (6) is unknown the dual reciprocity technique is utilised and the solution of the problem is expressed by the following system of nonlinear equations:

$$\mathbf{H} \varphi - \mathbf{G} \mathbf{Q}_\varphi = \frac{1}{\lambda_0} \sum_{j=1}^M \mathbf{B} \left(\mathbf{H} \hat{\mathbf{T}} - \mathbf{G} \hat{\mathbf{Q}} \right) \quad (7)$$

where $\hat{\mathbf{T}}$ and $\hat{\mathbf{Q}}$ contain vectors formed by the values of particular solution and its normal derivative, while \mathbf{B} is the vector which is found to satisfy DRM approximation at all nodes on the boundary and at all chosen internal points [8]. It is also proposed to use the same fundamental solution T^* , and consequently \mathbf{H} and \mathbf{G} , as for constant material properties. In this case approximated term (the right hand side of equation (7)) represents only value of difference between real material properties and assumed constant values for which elements of the influence matrices are calculated. Details of how to solve a such boundary problem were described in author's previous works.

The system of equations ((7) or (3)) is initially written separately for each phase. As long as one does not know the exact positions of solidus and liquidus the existing conditions on these interfaces (see Fig. 1) can not be fulfilled together. Therefore, conditions for temperature are weakened and along both fronts the compatibility conditions are subsequently applied, *i.e.* $T_L(\mathbf{r}) = T_M(\mathbf{r})$ or $T_M(\mathbf{r}) = T_S(\mathbf{r})$ where subscript M refers to mushy zone.

Three systems of equations, written for each subdomain, can be combined and one system is created from which temperatures on both interfaces are calculated. It is clear that as conditions along the interfaces are weakened, the calculated temperatures are different from the liquidus and solidus temperature respectively. Therefore, the positions of the solidus and liquidus are updated by the front tracking algorithm and the calculations stop when $T_L(\mathbf{r}) = T_L(\mathbf{r}) = T_{Lik}$ for $\mathbf{r} \in \Gamma_{DC}$ and $T_L(\mathbf{r}) = T_S(\mathbf{r}) = T_{Sol}$ for $\mathbf{r} \in \Gamma_{D'C'}$ within the required accuracy.

For the sake of improving efficiency of the algorithm (by decreasing the number of variables describing the location of interfaces) it is proposed to use Bezier splines. The coordinates of control points of these splines describe uniquely location of both interfaces and they become design variables. Consequently cubic elements are spun along any number of Bezier splines with smoothness enforced at each junction point. The way of forming Bezier splines is described in [1]. Generally, it can be concluded that control points create two straight lines to which the generated curve has to be tangent.

New positions of control points are found by minimization of the objective function, defined as:

$$\Delta = \sum_{i=1}^{N_L} (T_i^L - T_{Lik})^2 + \sum_{i=1}^{N_S} (T_i^S - T_{Sol})^2 \quad (8)$$

where N_L is the number of nodes on the liquidus, N_S is the number of nodes on the solidus, while the upper subscripts L and S indicate on which front node is situated.

Differentiation of the above function with respect to all design variables and expanding temperature T into Taylor series gives the following system of equations:

$$\mathbf{A} \mathbf{s} = \mathbf{B} \quad (9)$$

where \mathbf{A} and \mathbf{B} are the matrices which elements can be calculated from:

$$A_{kj} = \sum_{i=1}^{N_L} \frac{DT_i^P}{Ds_j} \frac{DT_i^P}{Ds_k} \quad \text{or} \quad A_{kj} = \sum_{i=1}^{N_S} \frac{DT_i^K}{Ds_j} \frac{DT_i^K}{Ds_k} \quad (10)$$

$$B_k = \sum_{i=1}^{N_L} \left(T_{Lik} - T_i^{Po} + \sum_{j=1}^M \frac{DT_i^P}{Ds_j} s_j^o \right) \frac{DT_i^P}{Ds_k} + \sum_{i=1}^{N_S} \left(T_K - T_i^{Ko} + \sum_{j=1}^M \frac{DT_i^K}{Ds_j} s_j^o \right) \frac{DT_i^K}{Ds_k} \quad (11)$$

while \mathbf{s} is the vector of design variables.

The total derivatives of temperature $\frac{DT_i}{Dv_m}$ are of great importance for the whole procedure. In the previous author's works, *e.g.* [3] it was shown how to calculate these quantities for continuous casting problems solved by BEM.

Numerical examples and conclusions

As already mentioned, previous authors' work, *e.g.* [3], demonstrate that front tracking algorithm utilising sensitivity coefficients is capable of solving the heat transfer problem in the continuous casting of pure metals to very high accuracy. It was particularly proved that only 2 – 4 Bezier segments are sufficient for a good approximation of the phase change front. Also the convergence process is considerably quicker than in other approaches. The main objective of calculations carried out in this work is to show that the same algorithm and computer code after slight modifications are capable of solving the continuous casting problem of alloys.

The first test case refers to continuous casting of steel. Adopted geometry, the most important material properties and boundary conditions are shown in Fig. 2.

Proposed algorithm converged to the final solution just in 25 iterations. In order to be able to verify obtained BEM numerical results, the same boundary problem was also solved using the one-domain method (also known as the enthalpy method) using commercial package Fluent. Since one can use in Fluent so-called the liquid fraction and only the linear elements, similar model of solidification was applied in BEM calculations. As it can be clearly seen in Fig. 2, the positions of the solidus and the liquidus obtained in both solutions are almost identical.

In next test case the continuous casting of aluminum alloy is analysed. The BEM numerical results obtained using the proposed algorithm were compared with the results of measurements made in EPFL, Lausanne, Switzerland [9]. As it is shown in Fig. 3 generally very good agreement was reached.

Results of calculations obtained using developed algorithm were also compared with the calculations made by the other researchers. In every case very good agreement was reached and it will be

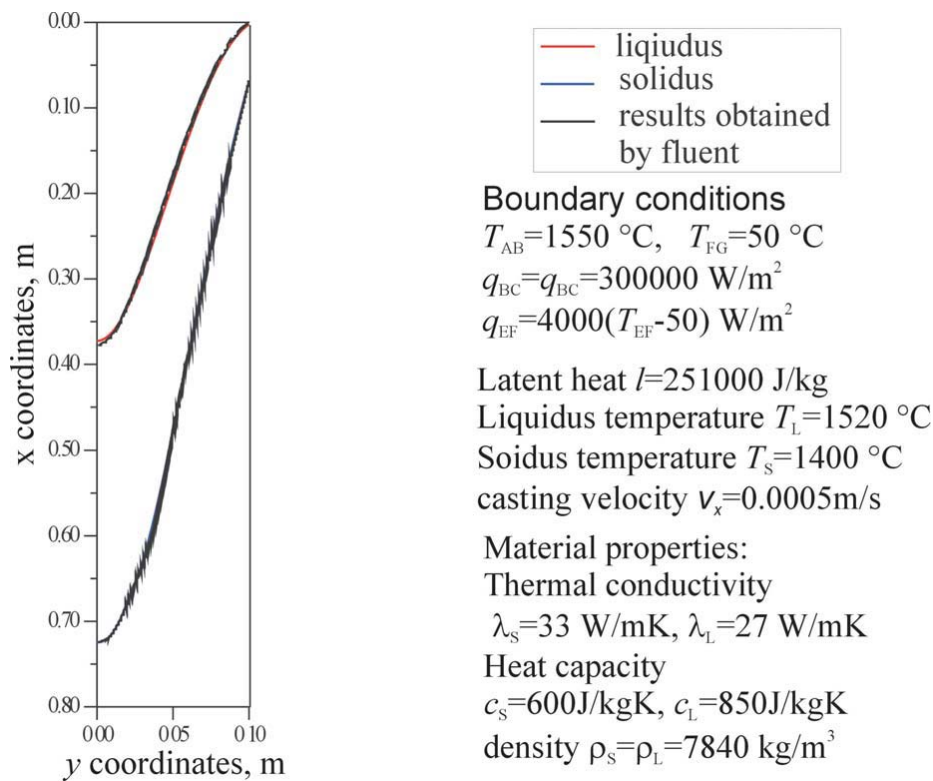


Figure 2: Comparison of results obtained by developed algorithm and in Fluent.

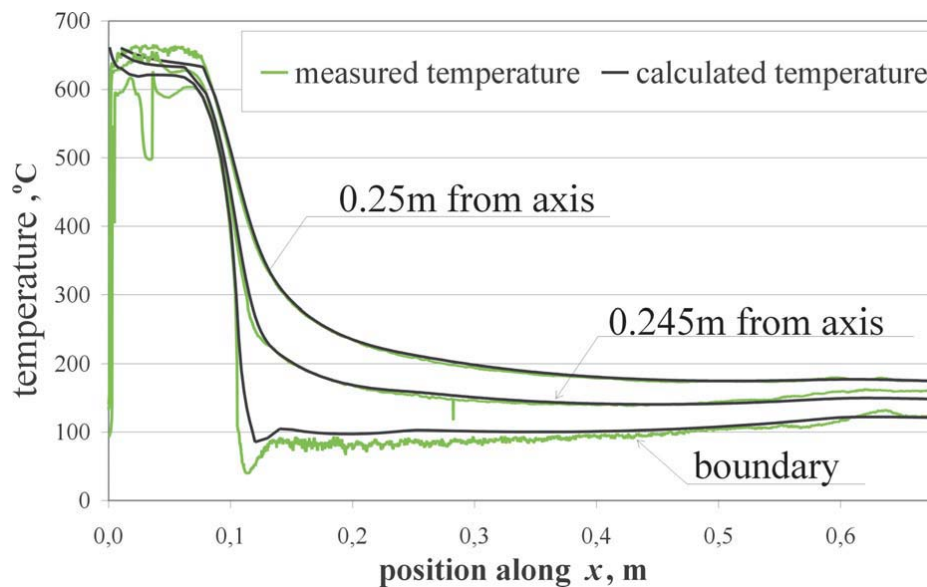


Figure 3: Comparison of measured and calculated temperatures.

demonstrated during the conference. The influence of the material nonlinearity on obtained results is generally similar to this found in a case of pure metals.

Acknowledgement

The financial assistance of the National Committee for Scientific Research, Poland, grant no 8 T10B 061 23, is gratefully acknowledged herewith.

References

- [1] Cholewa R., Nowak A. J., Bialecki R., Wrobel L. C., *Cubic Bezier splines for BEM heat transfer analysis of the 2-D continuous casting problems*, special issue of Computational Mechanics, Vol. 28, pp. 282–290, Springer-Verlag, 2002.
- [2] Cholewa R., Nowak A. J., Wrobel L. C., *Front tracking BEM solution of the heat transfer problem in the continuous casting process*, Fifth World Congress on Computational Mechanics, July 7-12, 2002, Viena, Austria, On-line publication (ISBN 3-9501554-0-6) <http://wccm.tuwien.ac.at/>
- [3] Cholewa R., Nowak A. J., Wrobel L. C., *Application of BEM and sensitivity analysis to the solution of the governing diffusion-convection equation for a continuous casting*, Special issue of Engineering Analysis with Boundary Element Method, Vol. 28, No. 4, pp. 389–403, 2004.
- [4] Das S. K., Sarkar A., *Computational modeling of thermal transport phenomena in continuous casting process based on non-orthogonal control volume approach*, Commun. Numer. Meth. Engng 12, pp. 657–671, 1996.
- [5] Fic A., Nowak A. J., Bialecki R., *Heat transfer analysis of the continuous casting process by the front tracking*, Engineering Analysis with Boundary Elements, Vol. 24, pp. 215-223, 2000.
- [6] Sarler B., Mencinger J., *Solution of temperature field in DC cast aluminium alloy billet by the dual reciprocity boundary element method*, International Journal of Numerical Methods for Heat & Fluid Flow, Vol. 9, No 3, pp. 269–295, 1999.
- [7] Sczygiol N., Szwarc G, *Application of enthalpy formulations for numerical simulation of casting solidification*, Computer Assisted Mechanics and Engineering Science, 8, pp. 99–120, 2001.
- [8] Wrobel L. C., Aliabadi M.H., *The Boundary Element Method*, Wiley, Chichester, 2002.
- [9] Drezet J.-M., Rappaz M., Grn G.-U., Gremaud M.: *Determination of Thermophysical Properties and Boundary Conditions of Direct Chill-Cast Aluminium Alloys Using Inverse Methods*, Metall. and Materials Trans. A, 2000, vol. 31A, pp.1627-1634.

Prediction of Oil Production of Individual Operator in a Multiple Leases Reservoir

M. N. Mohamad Ibrahim

School of Chemical Sciences, Universiti Sains Malaysia,
11800 Pulau Pinang, Malaysia, mnm@usm.my

Keywords: oil production rate; oil reservoir; multiple leases; drilling pattern; injector

Abstract. This paper presents a commonly existing problem in a multiple leases reservoir and tries to solve it using a boundary element method approach. The developed Boundary Element Method (BEM) formulation in calculating the productivity of well or clusters of wells located arbitrarily in an irregularly shaped reservoir was employed in this study to determine the total oil production for each operator that share a single reservoir. In this example application, two operators of equal area shared one circular oil reservoir. Different operator or section of the reservoir is assigned with different drilling pattern. The section that is developed with a four-spot drilling pattern produces 19% more oil compared to the section developed with a five-spot pattern. The case of adding injector wells into the system is also presented. Results showed that the difference between four-spot and five-spot patterns in term of oil production is less pronounce when injector wells were introduced to the system.

Introduction

Recently several major oil companies merged with each other in perusing their business. Besides to strengthen their capital and human resource, this step inevitable will help to minimize unnecessary court case that may occur among them especially when dealing with a multiple leases reservoir.

The multiple leases reservoir refers to a single oil reservoir that is having more than one operator working on it. This phenomenon can easily be seen in countries that have many small operators who have limited capital to bid for the whole lease. They will end up sharing the reservoir based on their working interest or the amount of capital that they are willing to invest.

While the boundary and the area of each operator can be specified on a map, one cannot be sure what is happening more than 1,000 feet underground follows exactly as what was planned earlier. Different drilling pattern for example will give different total oil production due to their differences in aerial sweep efficiency. This study presents a commonly existing problem among different operators in a multiple leases reservoir and tries to solve it using a boundary element method approach.

BEM Formulation

Differential equation describing the pressure distribution at all points in an oil reservoir is [1,2,3,4]:

$$\frac{\partial^2 p}{\partial X^2} + \frac{\partial^2 p}{\partial Y^2} + \frac{\mu}{k} \sum_{m=1}^{NSS} q_m \delta(X - X_m, Y - Y_m) = 0 \quad (1)$$

where p is pressure, μ is the dynamic viscosity of the fluid, k is the permeability, q_m is the flow rate of the m^{th} well per unit area (positive for injectors and negative for producers), δ is the Dirac delta function, X, Y are coordinates axes, and X_m, Y_m are coordinates of the m^{th} source and/or sink where m varies from 1 to NSS .

Eq (1) can be transformed into an integral equation by multiplying it with the free-space Green's function and integrating it twice by parts. The free-space Green's function, also called the fundamental solution [5] is given as:

$$G = \frac{1}{2\pi} \ln\left(\frac{1}{r}\right) \quad (2)$$

where r is the distance between a field point (X, Y) and a point of application of a unit charge (X_C, Y_C) . After standard manipulation [1], Eq (1) then becomes:

$$\alpha p(X_i, Y_i) = \frac{1}{2\pi} \sum_{j=1}^N \frac{\partial p}{\partial n_j} \int_{s_j} \ln\left(\frac{1}{r_{i,j}}\right) ds - \frac{1}{2\pi} \sum_{j=1}^N p_j \int_{s_j} \frac{\partial}{\partial n} \left[\ln\left(\frac{1}{r_{i,j}}\right) \right] ds + \frac{1}{2\pi} \frac{\mu}{k} \sum_{m=1}^{N_{SS}} q_m \ln\left(\frac{1}{r_{i,m}}\right) \quad (3)$$

where the boundary of the reservoir is divided into N constant elements with constant properties. α is the included angle at the i^{th} pivot point. It is assigned a value of $\frac{1}{2}$ when the pivot point is on a smooth boundary (*i.e.* not on a corner), and a value of 1 when the pivot point is inside the problem domain.

The integral equations are written for boundary points as well as for the locations of the point sources and/or sinks (producer and/or injector wells). A solution of the resulting equation gives the value of flow rate, q , for each of the well directly as well as the unknown boundary values of pressure p and pressure gradient dp/dn . The formulation was coded into a computer program namely FORTRAN which allows a rapid analysis process.

Example Application

Consider a hypothetical homogeneous circular oil reservoir having the following properties:

- $Area = 314.2 \times 10^6 \text{ feet}^2 = 7,212 \text{ acre}$ (reservoir area),
- $r_w = 0.25 \text{ feet}$ (well-bore radius),
- $k = 100 \text{ md}$ (absolute permeability), $\phi = 0.15$ (reservoir porosity),
- $h = 35 \text{ feet}$ (reservoir thickness),
- $\rho = 62.4 \text{ lb/ft}^3$ (reservoir fluid density),
- $\mu = 1.0 \text{ cp}$ (fluid viscosity), $p_w = 100 \text{ psi}$ (well-bore pressure),
- $p_e = 2,000 \text{ psi}$ (external reservoir pressure) and
- $Scale = 1: 5,000$

This newly discovered reservoir is going to be developed by two operators (A and B) at equal area. Different operator or section of the reservoir is assigned with different drilling pattern *i.e.* four-spot (B) and five-spot (A) drilling pattern respectively. Four-spot drilling pattern refers to a single pattern that is formed by four wells. The shape of the pattern is a triangle with one well located in the middle while the rest of the wells located each at the tip of the triangle. This pattern can be expanded side by side depending on the requirement. The same also true for the five-spot pattern where five wells are needed to form a single pattern of square shaped [6]. These patterns are shown in Fig. 1 where the solid lines connecting some of the wells represent the complete pattern whereas the dotted lines represent the incomplete pattern.

With the area of each pattern remain the same ($6.25 \times 10^6 \text{ feet}^2 = 143.5 \text{ acre}$) regardless of the pattern shape; each section of the reservoir is developed by 22 producer wells (the well that produces oil). The case of adding injector wells (the well that is used to inject or pump water into the reservoir in order to maintain the reservoir pressure) into the system is also presented. Four producer wells in each section of the reservoir are converted to injector wells. The injection rate was set to be 1,000 barrel of water per day. The location of these wells is shown in Fig. 2.

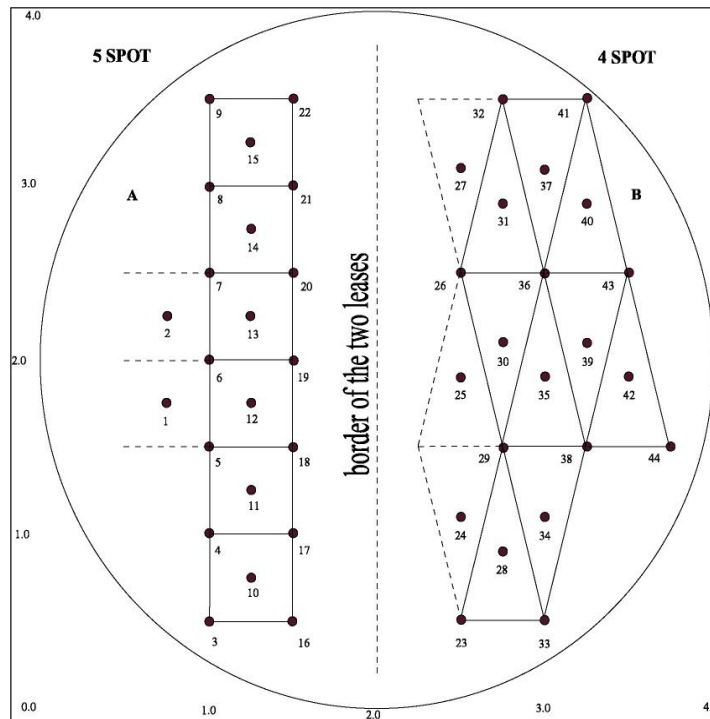


Fig. 1. Two operators of equal area shared one circular oil reservoir and developed the reservoir with two different drilling patterns

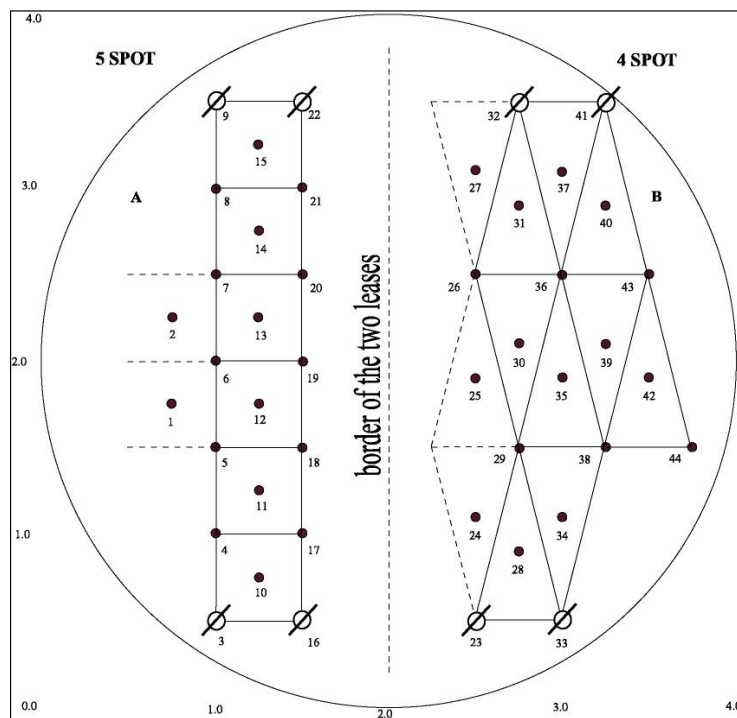


Fig. 2. Eight injector wells were introduced into the system

Results and Discussion

Complete simulation results obtained from the above studies in barrel per day (bbl/d) were compared and summarized in Table 1.

<i>Item</i>		<i>Operator A</i>	<i>Operator B</i>
Well Type	Drilling Pattern	5-spot	4-spot
All Producers	Total Oil Production, Q_n (bbl/d)	46,305	55,020
	Average Production per Well, Q_{avg} (bbl/d)	2,105	2,501
4 injector wells in each section	Total Oil Production, Q_n (bbl/d)	204,949	211,578
	Average Production per Well, Q_{avg} (bbl/d)	11,386	11,754

Table 1. Production data for two different operators

Obviously from Table 1, four-spot pattern is more superior compared to five-spot pattern in terms of Q_n and Q_{avg} . These results are consistent with previous study [7] in determining the optimum drilling pattern for a circular. Operator B in this case should feel very happy because he/she makes 19% more oil compared to his/her neighbor at the same amount of bid price. Although the area of each pattern (143.5 acre) was set to be the same as well as the number of wells (22) in each section of the reservoir, the number of complete pattern for these two drilling patterns is different. From Fig. 1, the number of complete pattern for the four-spot drilling pattern is nine whereas for the five-spot pattern is only six. Therefore, the four-spot pattern has the bigger aerial sweep efficiency compared to the five-spot pattern.

The difference in terms of total oil production as well as average production per well is less pronounce when injector wells were introduced to the system. This is because in this study, the injector wells were placed at about the same place in each section as if creating a giant five-spot pattern with several producer wells in the middle.

Depending on the initial agreement between these two parties (A and B), they may end up suing each other in the court if one person knows that the other person makes more money than him/her. This paper simply provides a way to solve this dispute if such problem occurs by determining how much of oil that each operator makes from different section in the same reservoir. This paper presents a case where different drilling patterns will result in different amount of oil production given that the area and the number of wells drilled are the same. This BEM formulation can handle a more complicated case than this one since the formulation is capable to give production rate of an individual well. Therefore one could tell the performance of each well present in the reservoir.

Conclusions

The result of this study could be used as a rule of thumb for reservoir engineers in the field when quick approximations need to be made. Although in the real life case, one could never obtained the exact numerical values as presented in the paper, it is believed that the real life case would follows the same general trend as the results of this study. History matching or actual production data matching step needs to be taken as in other reservoir simulation studies.

Other advantage of this BEM formulation is; it gives the production rate of an individual well. This will allow the operator to be able to identify those wells that are performing below expectation and subject them to remedial or work-over operations.

Acknowledgements

The authors would like to express their appreciations to Universiti Sains Malaysia for the financial support of this project. The author also would like to thank his beloved wife, Azah and his two princes Mohamad Aiman Hamzah and Ahmad Zaid for their supports, sacrifices and patience throughout this project.

References

- [1] D.T. Numbere and D. Tiab *An Improved Streamline-Generating Technique That Uses the Boundary (Integral) Element Method*, *SPE Reservoir Engineering*, Vol. 3(3), 1061-68, (1988).
- [2] M.N. Mohamad Ibrahim and D.T. Numbere *Boundary Element Analysis Of The Productivity Of Complex Petroleum Well Configurations*, In C.S. Chen, C.A. Brebbia and D. Pepper (Eds), *Boundary Element Technology XIII*, WIT Press, Southampton, 25-34 (1999).
- [3] M.N. Mohamad Ibrahim and D.T. Numbere *Productivity Predictions For Oil Well Clusters Using A Boundary Element Method*, *J. of Physical Science*, Vol.11, 148-157, (2000).
- [4] M.N. Mohamad Ibrahim and D.T. Numbere *Boundary Shape Effects On the Productivity of Oil Well Clusters*, In *Boundary Element Technology XIV*, A. Kassab and C. A. Brebbia (Eds), WIT Press, Southampton, 293-299 (2001).
- [5] C.A. Brebbia *The Boundary Element Method for Engineers*, John Wiley and Sons Inc., New York City, 46-103 (1978).
- [6] F.F. Craig *The Reservoir Engineering Aspects of Waterflooding*, Monograph Series, SPE, Richardson, Texas, 49 (1971).
- [7] M.N. Mohamad Ibrahim, J. Laeng @J. Abdullah and K.W. Kong *The Optimum Drilling Pattern for A Circular and A Rectangular Shaped Oil Reservoir*, *Proceedings of the 2nd World Engineering Congress*, Sarawak, Malaysia, 27-30 (2002).

An alternative method for solving steady free convection problems in porous media

A. Curteanu, D. B. Ingham, L. Elliott, D. Lesnic

Department of Applied Mathematics, University of Leeds, Leeds LS2 9JT, UK, anca@maths.leeds.ac.uk

Keywords: Laplacian decomposition; Boundary Element Method (BEM); Free convection, Porous media.

Abstract. Free convection in two-dimensional porous media is solved using a new approach based on a Laplacian decomposition, which in turn stems from Almansi decomposition. Basically it requires the solution of three Laplace equations for the temperature and two auxiliary harmonic functions. These equations, which become coupled through the boundary conditions, are numerically solved using the boundary element method (BEM). Numerical results are presented and discussed for a mathematical example exploring different types of boundary elements and using different combinations of the boundary conditions for non-smooth geometries.

Introduction

The governing equations for the problem of steady free convection in porous media are the Darcy, energy and continuity equations, see, for example, [1,2],

$$\underline{\bar{q}} = -\frac{K}{\mu}(\nabla \bar{P} - \rho \underline{g}) \quad (1)$$

$$(\underline{\bar{q}} \cdot \nabla) \bar{T} = \alpha_m \nabla^2 \bar{T} \quad (2)$$

$$\nabla \cdot \underline{\bar{q}} = 0 \quad (3)$$

where $\underline{\bar{q}}$ is the velocity vector, \bar{T} the temperature, \bar{P} the pressure, ρ the density, μ the coefficient of viscosity, K the permeability of the medium and α_m the effective thermal diffusivity of the medium.

Introducing the Boussinesq approximation

$$\rho = \rho_0(1 - \beta(\bar{T} - \bar{T}_0)) \quad (4)$$

where ρ_0 and T_0 are the reference density and temperature, respectively, and β is the coefficient of thermal expansion, results in equation (1) becoming

$$\underline{\bar{q}} = -\frac{K}{\mu}(\nabla \bar{P} - \rho_0(1 - \beta(\bar{T} - \bar{T}_0))\underline{g}) \quad (5)$$

Denoting a characteristic length, velocity and temperature by L , \bar{U}_0 and \bar{T}_R , respectively, together with the following non-dimensionalisation:

$$\bar{x} = Lx, \quad \underline{\bar{q}} = \bar{U}_0 \underline{q}, \quad \underline{g} = -g\underline{i}, \quad \bar{T} - \bar{T}_0 = \bar{T}_R T, \quad \bar{P} = -\rho_0 g x - \rho_0 \bar{U}_0^2 P \quad (6)$$

results in equations (2), (3) and (5) becoming

$$\underline{q} = \left(\frac{K \bar{U}_0}{\nu L} \right) \nabla P + \left(\frac{K \beta g \bar{T}_R}{\nu \bar{U}_0} \right) T \underline{i} \quad (7)$$

$$\left(\frac{\bar{U}_0}{\alpha_m L} \right) (\underline{q} \cdot \nabla) T = \nabla^2 T \quad (8)$$

$$\nabla \cdot \underline{q} = 0 \quad (9)$$

where $\nu = \frac{\mu}{\rho_0}$ is the kinematic viscosity, P is the non-dimensional pressure measured above the equilibrium value and the positive x direction is measured vertically upwards. Now assuming that the non-dimensional parameter $\frac{\bar{U}_0}{\alpha_m L}$ is small, so that the convective terms in the energy equation can be neglected, and that the characteristic velocity and temperature are defined to be $\frac{\nu L}{K}$ and $\frac{\nu^2 L}{K^2 \beta g}$,

respectively, then equations (7), (8) and (9) reduce to the following non-dimensional set of equations for the incompressible fluid motion and temperature in a porous medium, namely

$$\underline{q} = \nabla P + T\underline{i} \quad \text{or} \quad (u, v) = \left(\frac{\partial P}{\partial x}, \frac{\partial P}{\partial y} \right) + (T, 0) \quad (10)$$

$$\nabla^2 T = 0 \quad \text{or} \quad \frac{\partial^2 T}{\partial x^2} + \frac{\partial^2 T}{\partial y^2} = 0 \quad (11)$$

$$\nabla \cdot \underline{q} = 0 \quad \text{or} \quad \frac{\partial u}{\partial x} + \frac{\partial v}{\partial y} = 0 \quad (12)$$

where $\underline{q} = (u, v)$ and $\underline{i} = (1, 0)$.

Mathematical formulation

We now introduce the streamfunction ψ , with the x and y components of the fluid velocity defined by

$$u = \frac{\partial \psi}{\partial y} \quad \text{and} \quad v = -\frac{\partial \psi}{\partial x}. \quad (13)$$

Differentiating equation (10) with respect to x and y and y and x , respectively, and adding or subtracting them accordingly, together with the use of the continuity equation, then the following two relations are obtained

$$\nabla^2 P = -\frac{\partial T}{\partial x} \quad (14)$$

$$\nabla^2 \psi = \frac{\partial T}{\partial y}. \quad (15)$$

In order to simplify the equations (14) and (15), the following two combinations for the streamfunction and pressure are introduced

$$\psi = f + \frac{1}{2}yT \quad (16)$$

$$P = g - \frac{1}{2}xT \quad (17)$$

resulting in f and g being solutions of Laplace's equation, namely $\nabla^2 f = 0$ and $\nabla^2 g = 0$, i.e. the above substitutions have reduced the problem to the solution of three Laplace equations. A similar idea has been proposed by Jaswon and Symm, see [3,4], for solving the biharmonic equation.

The development of the BEM for discretizing the Laplace equation is the classical approach and it is based on using the fundamental solution for the Laplace equation which in two-dimensions is given by $G(q, q') = \ln|q - q'|$ and Green's identities, see, for example, [5].

Based on the BEM, we subdivide the boundary Γ into a series of N elements Γ_j , $j = \overline{1, N}$, and approximate the function f and its outward normal derivative f' at the collocation points of each boundary element Γ_j by f_j and f'_j , respectively. Thus the discretized boundary integral equation is given by:

$$\eta(q_i)f(q_i) = \sum_{j=1}^N \left[f'_j \int_{\Gamma_j} G(q_i, q') d\Gamma_{q'} - f_j \int_{\Gamma_j} G'(q_i, q') d\Gamma_{q'} \right], \quad i = \overline{1, N} \quad (18)$$

where $q' \in \Gamma$, $d\Gamma_{q'}$ denotes the differential increment of Γ at q' , $\eta(q) = 2\pi$ if $q \in \Omega$ and $\eta(q) =$ the internal angle between the tangents to Γ on either side of q if $q \in \Gamma$, and q_i is the centroid node of each element Γ_i when the BEM with constant elements (CBEM) is used. However, the points are placed at a quarter of each segment length from the segment endpoints when using BEM with discontinuous linear elements (DLBEM). Defining

$$A_{ij} = \int_{\Gamma_j} G(q_i, q') d\Gamma_{q'} \quad (19)$$

$$B_{ij} = \int_{\Gamma_j} G'(q_i, q') d\Gamma_{q'} + \eta(q_i)\delta_{ij} \quad (20)$$

where δ_{ij} is the Kronecker delta symbol, equation (18) reduces to the following system of N linear algebraic equations:

$$\sum_{j=1}^N [A_{ij}f'_j - B_{ij}f_j] = 0, \quad i = \overline{1, N}. \tag{21}$$

Similar equations are obtained also for \mathbf{g} and \mathbf{T} .

Now the mathematical formulation of the problem can be reduced to a system of $3N$ equations in $6N$ unknowns, i.e.

$$\begin{cases} A\mathbf{f}' - B\mathbf{f} = 0 \\ A\mathbf{T}' - B\mathbf{T} = 0 \\ A\mathbf{g}' - B\mathbf{g} = 0 \end{cases} \tag{22}$$

and $3N$ appropriate boundary conditions. This system of equations can be solved using, for example, a Gaussian elimination procedure.

In this study we consider two cases in which two different boundary conditions are specified over the whole boundary of the solution domain. The remaining N equations necessary to solve the system of equations are obtained for each case from Darcy's equation in the direction normal or tangential to the boundary, according to whether ψ or P is prescribed on the boundary.

Numerical Results

We will illustrate the numerical results considering one test example, namely the analytical expressions for the three harmonic functions are given by:

$$f^{(an)} = x^2 - y^2 - x^2y/2 + y^3/6 \tag{23}$$

$$g^{(an)} = -2xy + x^3/6 - xy^2/2 \tag{24}$$

$$T^{(an)} = x^2 - y^2 \tag{25}$$

with the corresponding streamfunction and pressure given by:

$$\psi^{(an)} = x^2 - y^2 - y^3/3 \tag{26}$$

$$P^{(an)} = -2xy - x^3/3 \tag{27}$$

in a simple two-dimensional non-smooth geometry, with corners, namely the unit square $\Omega = \{(x, y) | -\frac{1}{2} \leq x \leq \frac{1}{2}, -\frac{1}{2} \leq y \leq \frac{1}{2}\}$. We want to mention that the same example has been used for investigating the same problem in a smooth domain, namely a circle, with different boundary conditions, see [6].

Further, different numbers of *constant* and *discontinuous linear* boundary elements are used in order to provide simultaneously the boundary values for f, f', T, T', g and g' . These boundary values are used to determine the solution for f, g and T inside the domain Ω explicitly using integral equations, such as (18). Once these values have been obtained accurately then the corresponding functions P and ψ on both the boundary and inside the domain Ω can be determined using equations (16) and (17).

In most practical situations we would expect ψ and T to be specified on the boundary and in such circumstances then the normal derivative of P can be established on the boundary. Hence this, together with P prescribed at a point is expected to result in a well posed problem. However, the same is not so clear for other similar combinations of ψ, ψ', P, P', T and T' on the boundary. In what follows we also investigate what addition information, if any, is required to establish a well posed problem when different combinations of two of these quantities are prescribed on the boundary.

ψ and T specified on the boundary. In this subsection we consider the solution of the problem under investigation with the streamfunction and the temperature specified on the boundary Γ . The other N equations necessary to solve the system are obtained by differentiating equation (17) with respect to n , resulting in $\frac{\partial g}{\partial n} - \frac{\partial(x/2)}{\partial n}T - \frac{x}{2} \frac{\partial T}{\partial n} = \frac{\partial P}{\partial n}$. Since T and ψ are given on the boundary, $\frac{\partial P}{\partial n}$ can

be determined either analytically or by using finite differences from the normal derivative of the normal component of pressure, which can be expressed directly in terms of temperature and the tangential derivative of the known tangential component of streamfunction using equation (10) together with equation (13).

The problem can be now described mathematically by equations (22) together with the following boundary conditions:

$$\left. \begin{aligned} f + \frac{y}{2}T &= \psi^{(an)} \\ T &= T^{(an)} \\ g' + h_1 T - \frac{x}{2}T' &= P' \end{aligned} \right\} \text{ on } \Gamma \quad (28)$$

where $h_1 = \frac{\partial(x/2)}{\partial n}$.

The solution of this problem is clearly not unique since an arbitrary constant may be added to g . In order to overcome this, let us assume that the pressure can be measured at one point on the boundary. Since T is already prescribed over the whole boundary, that means that g can be found at the point where P is given, see equation (17). Thus g is uniquely determined. Since ψ and T are specified all over the boundary then from (16) the uniqueness in f is ensured.

The numerical results obtained, using either the CBEM or DLBEM, are in good agreement with the analytical solution for predicting both the unspecified boundary data and the streamfunction and the pressure inside the domain. The results for the streamfunction inside the solution domain are graphically represented in Figure 1(a). Moreover, the numerical solutions for the harmonic functions on the boundary are completely free of oscillations even when CBEM are used, see Figure 1(b) for the variation of f as a function of ζ , i.e. the fraction of the number of boundary elements measured anti-clockwise round the boundary from the point $(-\frac{1}{2}, \frac{1}{2})$ to the total number of boundary elements.

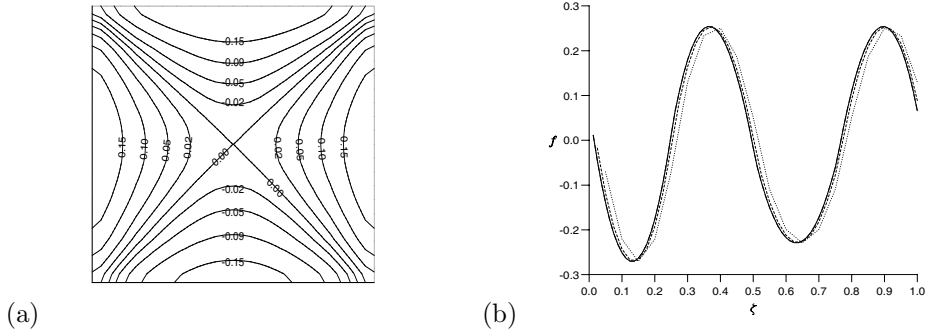


Figure 1: (a) The numerical interior solution for ψ using the BEM with $N = 80$ (- · - · - ·) *constant* boundary elements and (b) the numerical boundary solution for f using the BEM with $N = 20$ (···), $N = 40$ (- - -) and $N = 80$ (- · - · - ·) *constant* boundary elements and the analytical solution (—) with ψ and T specified on the boundary.

ψ and P specified on the boundary. In this subsection we consider the solution for the problem with the streamfunction and the pressure specified on the boundary Γ . Since both ψ and P are known, then in order to provide the other N equations necessary to solve the full system, we can use either the equation $\frac{\partial g}{\partial n} - \frac{\partial(x/2)}{\partial n}T - \frac{x}{2}\frac{\partial T}{\partial n} = \frac{\partial P}{\partial n}$ or $\frac{\partial f}{\partial n} + \frac{\partial(y/2)}{\partial n}T + \frac{y}{2}\frac{\partial T}{\partial n} = \frac{\partial \psi}{\partial n}$.

(a) **Boundary conditions in terms of g' , T and T' .** The unknown functions are obtained as the solution of the system of equations (22), subject to the following boundary conditions:

$$\left. \begin{aligned} f + \frac{y}{2}T &= \psi^{(an)} \\ g - \frac{x}{2}T &= P^{(an)} \\ g' + h_1 T - \frac{x}{2}T' &= P' \end{aligned} \right\} \text{ on } \Gamma \quad (29)$$

Solving the resulting system of linear algebraic equations, we observed that the numerical solutions for the harmonic functions are no longer a representation of the corresponding analytical solutions.

Uniqueness of the solution. Let f_0, g_0 and T_0 be solutions of the problem. The transformation $T = T_0 + a$ implies the transformations $f = f_0 - \frac{ay}{2}$ and $g = g_0 + \frac{ax}{2}$, where a is an arbitrary constant. So setting the value of T at one point should be enough to ensure a unique solution. Unfortunately, the numerical solution did not indicate this. Hence, we imposed the values of T at two different points $(x_1, y_1), (x_2, y_2)$ on the boundary. We observed that these two points can be chosen such as $x_1 \neq x_2$ or $x_1 = x_2 = 0$ or $y_1 \neq y_2$ or $y_1 = y_2 = 0$ to provide a unique solution.

By imposing the values of T at two points on the boundary such that $x_1y_2 \neq x_2y_1$, the solution of the system (22) subject to the boundary conditions (29) was undertaken employing discretizations comprising 20, 40 and 80 constant and discontinuous linear boundary elements, respectively. The numerical results obtained for ψ and P inside the domain are accurately predicted in comparison with their analytical solution as can be seen for ψ in Figure 2. Although when using CBEM, the solution

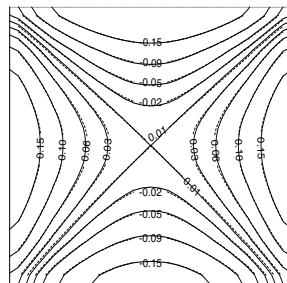


Figure 2: The numerical interior solution for ψ using the BEM with $N = 80$ (---) constant boundary elements and the analytical solution (—) with ψ and P specified on the boundary in case (a).

for the harmonic functions is subject to oscillations on the boundary, see Figure 3(a), when using DLBEM these oscillations disappear and the numerical solution become indistinguishable from the analytical solution for $N = 80$, see Figure 3(b) for T .

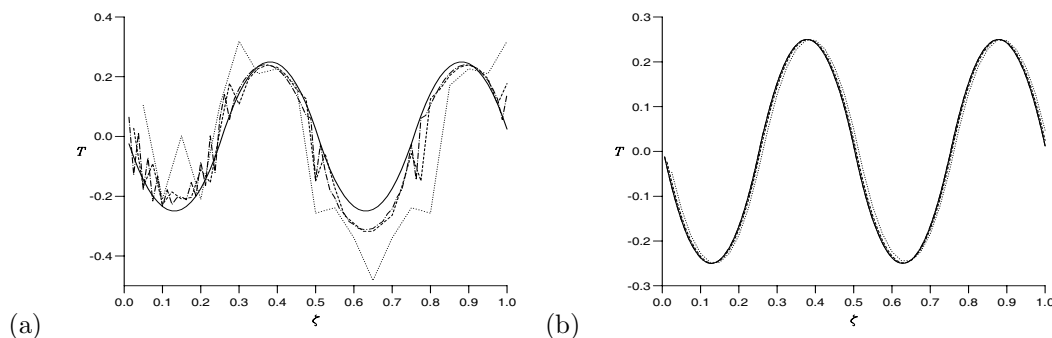


Figure 3: The numerical boundary solution for T using the BEM with $N = 20$ (···), $N = 40$ (---) and $N = 80$ (-·-·-·) (a) constant boundary elements and (b) discontinuous linear boundary elements and the analytical solution (—) with ψ and P specified on the boundary in case (a).

(b) Boundary conditions in terms of f', T and T' . By replacing the last boundary condition in the system (29) with a similar condition involving f', T and T' and setting the values of T at two

different points, the same behaviour as observed for the case (a) was obtained, but the accuracy is not as good. It is important to note that for this case the oscillations in f and g are larger than for the case (a) when using CBEM.

The oscillations for the harmonic functions, which in this case appear on the other two sides of the square from those in case (a), can be removed by imposing T at two different points on the boundary and using DLBEM. However, even if the oscillations completely disappear for f and g , they still remain, albeit with a very small amplitude for T . In addition, it is important to note that the remaining oscillations in T vanish when moving the square parallel with the coordinates axes until the origin is outside of the solution domain.

Although not presented in this paper, it is important to note that different other combinations on the boundary, namely (P, T) , (ψ, ψ') , and different combinations of ψ, P, T, ψ' on different parts of the boundary have been used. Normally in physical applications it is easier to measure pressure and temperature rather than both components of the fluid velocity, but for completeness we have considered this situation as well. Dealing with the non-uniqueness and the corners as appropriate, the numerical results obtained were in good agreement with their corresponding analytical solutions.

Conclusions

A novel numerical technique which is based on a Laplacian decomposition has been introduced. A physical problem, namely that of steady free convection in porous media has been considered in order to investigate the applicability of the method to non-smooth geometries.

The oscillatory behaviour for f, g and T on the boundary depends on both the type of boundary conditions which are used and the position of the origin of the coordinates in regard to the non-smooth domain. This study suggests that the use of discontinuous linear boundary elements for the square domain with the origin of coordinates outside of the domain is the most appropriate choice.

Regardless the position of the origin of the coordinates, non-uniqueness of the solution for f, g and T on the boundary was observed, while the uniqueness of the solutions ψ and P was retained.

By imposing the necessary conditions in order to obtain a unique solution and using higher order interpolation functions where required, we have obtained accurate solutions for f, g, T, ψ and P on the boundary and also for ψ and P in the interior of the solution domain using different combinations of the boundary conditions.

As expected, the accuracy of the results improves by increasing the number of boundary elements used to discretise the boundary of the solution domain.

Acknowledgement. A. Curteanu would like to acknowledge the financial support received from the ORS and the Department of Applied Mathematics at the University of Leeds.

References

- [1] A. Bejan, *Convective Heat Transfer in Porous Media*, Wiley, New York (1987).
- [2] I. Pop and D. B. Ingham, *Convective Heat Transfer: Mathematical and Computational Modelling of Viscous Fluids and Porous Media*, Pergamon, Oxford (2001).
- [3] M. A. Jaswon, M. Maiti and G. T. Symm, Numerical biharmonic analysis and some applications, *Int. J. Solids Structures* **3**, 309–332 (1967).
- [4] G.T. Symm, PhD Thesis, *Integral equation methods in elasticity and potential theory*, University of London (1964).
- [5] C. A. Brebbia, J. C. F. Telles and L. C. Wrobel *Boundary Element Technique: Theory and Applications in Engineering*, Springer-Verlag, Berlin (1984).
- [6] A. Curteanu, D. B. Ingham, L. Elliott and D. Lesnic, Laplacian decomposition of steady free convection in porous media, in D. B. Ingham *et al.* (eds.), *Emerging Technologies and Techniques in Porous Media*, Kluwer Academic Publishers, Netherlands, 119–129 (2004).